1

RBF-based multiscale control volume method for second order elliptic problems with oscillatory coefficients

D.-A. An-Vo, C.-D. Tran, N. Mai-Duy and T. Tran-Cong

Computational Engineering and Science Research Centre, Faculty of Engineering and Surveying, The University of Southern Queensland, Toowoomba, Queensland 4350, Australia.

Abstract: Many important engineering problems have multiple-scale solutions. Thermal conductivity of composite materials, flow in porous media, and turbulent transport in high Reynolds number flows are examples of this type. Direct numerical simulations for these problems typically require extremely large amounts of CPU time and computer memory, which may be too expensive or impossible on the present supercomputers. In this paper, we develop a high order computational method, based on multiscale basis function approach and integrated radial-basis-function (IRBF) approximant, for the solution of multiscale elliptic problems with reduced computational cost. Unlike other methods based on multiscale basis function approach, sets of basis and correction functions here are obtained through C^2-continuous IRBF element formulations. High accuracy and efficiency of this method are demonstrated by several one- and two-dimensional examples.

1 Introduction

In composite materials, the presence of particles/fibres in the resin gives rise to the multiscale fluctuations in the thermal or electrical conductivity. In porous media, formation properties, e.g. permeability, have a very high degree of spatial variability. These effects are typically captured at scales that are too fine for direct numerical simulation. To enable the solution of these problems, a number of advanced numerical methods have been developed. Examples include those based on the homogenisation theory (e.g. Dykaar and Kitanidis (1992)), upscaling methods (e.g. McCarthy (1995)) and multiscale methods (e.g. Hou and Wu (1997)). The homogenisation-theory-based methods have been successfully applied for the prediction of effective properties and statistical correlation lengths for multicomponent random media. However, restrictive assumptions on the media, such as scale separation and periodicity, limit their range of application. Furthermore, when dealing with problems having many separate scales, they become very expensive because their computational cost increases exponentially with the number of scales. For upscaling methods, their design principle is based on simple physical and/or mathematical motivations. A heterogeneous medium is replaced by a homogeneous

2

medium characterised by equivalent properties, and coarse scale equations are prescribed in explicit form. Although upscaling techniques are effective, most of their applications have been reported for the case of periodic structures. As opposed to upscaling, multiscale methods consider the full problem with the original resolution. The coarse scale equations are formed and solved numerically, where one constructs the basis functions from the leading order homogeneous elliptic equation in coarse scale elements. The idea of using the non-polynomial multiscale approximation space rather than the standard piecewise polynomial space was first introduced by Babuška, Caloz, and Osborn (1994) for one-dimensional problems and by Hou and Wu (1997); Hou, Wu, and Cai (1999) for two-dimensional elliptic problems. These methods have the ability to capture accurately the effects of fine scale variations without the need for using global fine meshes. Multiscale methods can be categorised into multiscale finite-element methods (MFEM) (e.g. Allaire and Brizzi (2005); Hou (2005)), mixed MFEM (e.g. Aarnes, Kippe, and Lie (2005); Arbogast (2002)) and multiscale finite-volume methods (MFVM) (e.g. Chu, Efendiev, Ginting, and Hou (2008); Jenny, Lee, and Tchelepi (2003)). Typically, there are two different meshes used: a fine mesh for computing locally the basis function space, and a coarse mesh for computing globally the solution of an elliptic partial differential equation (PDE). The multiscale bases are independent of each other and their constructions can thus be conducted in parallel. In solving the elliptic PDE, one may only need to employ a mesh that today's computing resources can efficiently and effectively handle. For two-scale periodic structures, Hou, Wu, and Cai (1999) have proved that the MFEM indeed converges to the correct solution independent of the small scale in the homogenisation limit. Multiscale techniques require the solutions of elliptic PDEs which are achieved by means of discretisation schemes.

Radial-basis-function networks (RBFNs) are known as a powerful tool for the approximation of scattered data. Their application to the solution of PDEs has received a great deal of attention over the last 20 years (e.g. Fasshauer (2007) and references therein). It is easy to implement RBF collocation methods and such methods can give a high order convergence solution. RBF-based approximants can be constructed through a conventional differentiation process, e.g. Kansa (1990), or an integration process (IRBF), e.g. Mai-Duy and Tran-Cong (2001, 2003). The latter (a smoothing operator) has several advantages over the former, including (i) to avoid the reduction in convergence rate caused by differentiation and (ii) to improve the numerical stability of a discrete solution. A number of IRBF approaches, based on local approximations (Mai-Duy and Tran-Cong, 2009), domain decompositions (Mai-Duy and Tran-Cong, 2008) and preconditioning schemes (Mai-Duy and Tran-Cong, 2010), have been presented towards the solution of large-scale problems. Re-

cently, a local high order approximant based on 2-node IRBF elements (a smallest IRBF set ever used for constructing approximants) has been proposed by An-Vo, Mai-Duy, and Tran-Cong (2010, 2011a). It was shown that such IRBF elements (IRBFEs) lead to a C^2-continuous solution rather than the usual C^0-continuous solution. IRBFEs have been successfully incorporated into the subregion-collocation (An-Vo, Mai-Duy, and Tran-Cong, 2011b) and point-collocation (An-Vo, Mai-Duy, and Tran-Cong, 2011b; An-Vo, Mai-Duy, Tran, and Tran-Cong, 2013) formulation for simulating highly nonlinear flows accurately and effectively. We also use IRBFEs to model strain localisation in (An-Vo, Mai-Duy, Tran, and Tran-Cong, 2012).

This paper is concerned with the incorporation of IRBFEs and subregion collocation (i.e. control-volume (CV) formulation) into the non-polynomial approximation space approach for solving one- and two-dimensional multiscale elliptic problems. Unlike other multiscale CV methods in the literature, sets of basis and correction functions in the present RBF-based multiscale CV method are obtained through highly accurate C^2-continuous IRBFE-CV formulations. As a result, not only the field variable but also its first derivatives are reconstructed directly with high accuracy. This is an important issue since the first derivatives contain information of great practical interest, such as the stress distribution and heat flux in composite materials or the flow velocity field in porous media.

The remainder of the paper is organised as follows. Section 2 defines the problem. Section 3 and 4 briefly review the multiscale finite element and finite volume methods, respectively, for the problem. The proposed method is described in Section 5 and numerical results are discussed in Section 6. Section 7 concludes the paper.

2   Problem definition

We consider the following multiscale elliptic problem

$$-\nabla \cdot (\lambda \nabla u) = f \ \text{ in } \ \Omega, \tag{1}$$

with appropriate boundary conditions. λ is a complex multiscale coefficient tensor; f a given function. Assume that the finest scale in λ is represented by ε.

3   Multiscale finite-element methods (MFEM)

Conventional discretisation techniques using piecewise polynomial approximation spaces can be applied to solve (1). However, it would require the mesh size h be much smaller than the finest scale, i.e. $h \ll \varepsilon$. In contrast, the multiscale computational framework which was firstly proposed by Hou and Wu (1997); Hou, Wu, and Cai (1999) uses a coarse grid of size $h > \varepsilon$ and basis functions which aim to adapt to

4

the small-scale features of the oscillatory coefficient tensor λ). The formulation of Hou and Wu (1997); Hou, Wu, and Cai (1999), namely the multiscale finite element method (MFEM), is based on a finite element framework where both the local and global problems are solved by a linear finite element method (LFEM). The MFEM is highly efficient and capable of capturing the large scale solution without resolving all the small scale details. For the case of two-scale periodic structures, it has been proved in Hou, Wu, and Cai (1999) that the MFEM indeed converges to the correct solution independent of the small scale in the homogenisation limit. However, for general cases e.g. non-periodic and random-scale media, the convergence of MFEM is not always guaranteed. In addition, there is an error gap between the MFEM solution and a corresponding fine scale reference solution. This error gap typically comes from two sources: (i) reduced problem boundary conditions for solving basis functions which is empirical even though an over-sampling technique has been proposed (Hou and Wu, 1997); and (ii) local homogeneous elliptic problems for basis functions. Due to the latter the basis functions do not involve effects of the right hand side field f. The right hand side, in a manner similar to that in the MSFV method (discussed next), is only considered in the global coarse mesh system.

4   Multiscale finite volume (MSFV) method

Based on the multiscale basis function approach (Hou, Wu, and Cai, 1999; Hou and Wu, 1997), Jenny, Lee, and Tchelepi (2003) and Chu, Efendiev, Ginting, and Hou (2008) proposed the MSFV method for elliptic problems in subsurface flow simulation. Equation (1) governs the pressure field p as

$$-\nabla \cdot (\lambda \nabla p) = f \text{ in } \Omega, \tag{2}$$

with the boundary conditions $\nabla p \cdot \mathbf{n} = q$ and $p(\mathbf{x}) = g$ on $\partial\Omega_1$ and $\partial\Omega_2$, respectively. Note that $\partial\Omega = \partial\Omega_1 \cup \partial\Omega_2$ is the whole boundary of the domain Ω and $\mathbf{n}$ is the outward unit vector normal to $\partial\Omega$. The mobility tensor λ (permeability, $\mathbf{K}$, divided by the fluid viscosity, μ) is positive definite and the right-hand side f, q, and g are specified fields. The permeability heterogeneity is a dominant factor in dictating the flow behavior in natural porous formations. The heterogeneity of $\mathbf{K}$ is usually represented as a complex multiscale function of space. Resolving the spatial correlation structures and capturing the variability of permeability requires highly detailed description.

The MSFV method aims to efficiently compute the approximate solution of problem (2) for highly heterogeneous coefficient λ and source term f. The method can be explained as a cell-centered finite-volume method (Jenny, Lee, and Tchelepi, 2003) or a vertex-centered finite-volume method (Chu, Efendiev, Ginting, and

Hou, 2008). We present the latter here. A Cartesian grid of $N \times N$ is employed to represent the problem domain Ω (solid lines in Fig. 1), from which I ($I = (N-2) \times (N-2)$) non-overlapping control volumes $\overline{\Omega}_k$ associated with I interior grid points $\mathbf{x}_k$ ($k \in [1, I]$) are formed. This set of control volumes constitutes a grid which is referred to as the coarse grid (dashed black lines in Fig. 1). In addition, let $\widetilde{\Omega}$ be a collection of J cells $\widetilde{\Omega}^l$ ($l \in [1, J], J = (N-1) \times (N-1)$) defined by the original $N \times N$ Cartesian grid (solid lines in Fig. 1). This set of J cells is referred to as the dual coarse grid. Note that these two grids can be much coarser than the underlying fine grid (dashed green lines in Fig. 1 wherein each dual cell $\widetilde{\Omega}^l$ is discretised by a local fine grid of $n \times n$) on which the mobility field is represented. On each dual cell $\widetilde{\Omega}^l$, we seek the approximate solution $\widetilde{p}$ of p in the form

$$p^l \approx \widetilde{p}^l = \sum_{i=1}^{4} p_i^l \phi_i^l, \tag{3}$$

where p_i^l and ϕ_i^l are the pressure value at and the basis function associated with the node x_i^l, respectively, of the dual coarse cell $\widetilde{\Omega}^l$.

Unlike conventional discretisation methods, these basis functions $\{\phi_i^l\}_{i=1}^4$ are generated from solving the following leading order homogeneous elliptic equations on the dual coarse cell $\widetilde{\Omega}^l$,

$$\nabla \cdot (\lambda \nabla \phi_i^l) = 0 \text{ in } \widetilde{\Omega}^l. \tag{4}$$

Boundary conditions for (4) are derived from the requirement that $\phi_i^l(\mathbf{x}_j^l) = \delta_{ij}$ ($i, j \in [1, 4]$) and (4) be well-posed problems. Jenny, Lee, and Tchelepi (2003) employed the proposition in (Hou, Wu, and Cai, 1999) by solving reduced local one-dimensional problems to specify the boundary conditions for (4). The elliptic problems (4) in $\widetilde{\Omega}^l$ with such boundary conditions can be solved by any appropriate numerical method. In order to obtain a solution that depends linearly on the nodal pressures p_i^l as in (3), we solve four elliptic problems, one for each nodal pressure.

To derive a linear system for the nodal pressure values p_k, we substitute expressions (3) for $\widetilde{p}$ in the four dual cells associated with $\mathbf{x}_k$ into equation (2) and integrate over $\overline{\Omega}_k$, which leads to

$$-\int_{\overline{\Omega}_k} \nabla \cdot (\lambda \nabla \widetilde{p}) \mathrm{d}\Omega = -\int_{\overline{\Omega}_k} \nabla \cdot \left(\lambda \nabla \left(\sum_{l=1}^{4} \sum_{i=1}^{9} \phi_i^l p_i \right) \right) \mathrm{d}\Omega = \int_{\overline{\Omega}_k} f \mathrm{d}\Omega, \tag{5}$$

where the indices l and i refer to local dual cells and local nodal points, respectively, associated with $\mathbf{x}_k$ and $\mathbf{x}_k \equiv \mathbf{x}_1$ as shown in Fig. 2. Note that in the summation $\sum_{i=1}^{9} \phi_i^l p_i$ the index i of the basis functions ϕ_i^l only takes on the four values relevant

6

to $\widetilde{\Omega}^l$ (i.e. $\phi_i^l = 0$ otherwise). Applying the Gauss theorem to equation (5), one obtains

$$-\int_{\partial\overline{\Omega}_k}\left(\lambda\nabla\left(\sum_{l=1}^{4}\sum_{i=1}^{9}\phi_i^l p_i\right)\right)\cdot\mathbf{n}_k\mathrm{d}\Gamma = \sum_{i=1}^{9}p_i\sum_{l=1}^{4}\int_{\partial\overline{\Omega}_k}\left(-\lambda\nabla\phi_i^l\right)\cdot\mathbf{n}_k\mathrm{d}\Gamma = \int_{\overline{\Omega}_k}f\mathrm{d}\Omega,$$

(6)

where $\mathbf{n}_k$ is the outward unit vector normal to $\partial\overline{\Omega}_k$. Equations (6) at a nodal point $\mathbf{x}_k$ ($k \in [1,I]$) can be written in matrix form as

$$A_{ki}p_i = b_k \tag{7}$$

for the nodal pressure values p_k with

$$A_{ki} = \sum_{l=1}^{4}\int_{\partial\overline{\Omega}_k}\left(-\lambda\nabla\phi_i^l\right)\cdot\mathbf{n}_k\mathrm{d}\Gamma \tag{8}$$

and

$$b_k = \int_{\overline{\Omega}_k}f\mathrm{d}\Omega. \tag{9}$$

We can reconstruct the fine scale pressure $\widetilde{p}^l$ in each dual coarse cell $\widetilde{\Omega}^l$ with p_k and the approximation (3). Implementing the reconstruction on the whole problem domain Ω one obtains the fine scale pressure $\widetilde{p}$, which is an approximation of the pressure field p.

Although the MSFV approach strongly resembles the multiscale finite element method by Hou, Wu, and Cai (1999), i.e. the construction of the basis functions is almost identical, the MSFV is a finite-volume method and hence conservative. In some applications such as single and multiphase flows through porous media one is also interested in accurately representing the small-scale velocity field. Chen and Hou (2002) provide clear evidences that a locally conservative fine scale velocity field is a necessary requirement for accurate modeling of fluid transport. To construct the fine scale flow field, a straightforward way would be to use the basis functions in (3), but then the reconstructed fine scale velocity field is in general discontinuous at the interfaces of the dual cells. Therefore, large errors can occur in the divergence field, and local mass balance is violated. Jenny, Lee, and Tchelepi (2003) describe how to reconstruct a conservative fine scale velocity field through the obtained pressure field $\widetilde{p}$. The reader is referred to this work for more details.

The efficiency of the MSFV method for large scale problems comes from the fact that fine scale details are captured through solving local problems (4) on small dual

cells for basis functions. This step is a preprocessing step and has to be done once only. Furthermore, the construction of the fine scale basis functions is independent from cell to cell and therefore perfectly suited for parallel computation.

The MSFV method was firstly used for solving single-phase flow in homogeneous and heterogenous permeability fields in (Jenny, Lee, and Tchelepi, 2003). Jenny, Lee, and Tchelepi (2004) and Jenny, Lee, and Tchelepi (2006) extended the method to time dependent problems in incompressible two-phase flows where the explicit and implicit time integrations were presented respectively. Lunati and Jenny relaxed the incompressible constraint in (Lunati and Jenny, 2006a) and compressible multiphase flow models were solved. It is important to note that until this stage of development the MSFV method basically was not designed to solve elliptic problems with complex source terms and not appropriate to account for gravity and capillary pressure effects. The reason is that the basis functions and their linear combinations are solutions of local homogenous elliptic problems (4). The right hand side of the governing equation (2) is only taken into account in the coarse grid linear system (7). This led to the idea of introducing correction functions in (Lunati and Jenny, 2006b, 2008). Unlike basis functions ϕ_i^l, correction functions p_c^l are the solutions of local elliptic problems on the dual cells with the right hand side f, i.e.

$$\nabla \cdot (\lambda \nabla p_c^l) = f \ \text{ in } \ \widetilde{\Omega}^l. \tag{10}$$

At the grid nodes $\mathbf{x}_k$ which belong to $\widetilde{\Omega}^l$, we impose $p_c^l(\mathbf{x}_k) = 0$. The boundary conditions of (10) on the edge segments of the dual cell can be obtained in a manner similar to those in (4), i.e. by solving reduced local one-dimensional problems. It has been shown for a wide range of challenging test cases that these reduced problem boundary conditions provide a good localisation assumption. There exist scenarios, however, which demonstrate some limitations of these boundary conditions. Specifically, the MSFV solution with correction functions and global fine scale reference solution p_f (p_f is an approximation of p on the global fine grid) are identical only if the basis and correction functions happen to capture the exact fine scale pressure solution on the interfaces of the dual coarse cells , i.e.

$$p_f^l = \sum_{i=1}^{4} p_i^l \phi_i^l + p_c^l \ \text{ on } \ \partial\widetilde{\Omega}^l. \tag{11}$$

It is desirable to approach boundary conditions for local elliptic problems via (11) instead of the reduced problem boundary conditions. Hajibeygi, Bonfigli, Hesse, and Jenny (2008) made it possible through an iterative framework based on a two-grid algorithm. At a step n with an initial pressure field $\widetilde{p}^{(n)}$, they perform several smoothing steps on the global fine grid to obtain a temporary reference solution

$\widetilde{p}_s^{(n)}$. This smoothed pressure field yields the boundary values of correction functions on each dual cell through (11) with p_f^l replaced by $\widetilde{p}_s^{(n)}$, i.e.

$$p_c^l = \widetilde{p}_s^{l(n)} - \sum_{i=1}^{4} p_i^l \phi_i^l \ \text{ on } \ \partial \widetilde{\Omega}^l, \tag{12}$$

where the boundary values of the basis functions ϕ_i^l on the dual cells are still obtained from the reduced problem boundary conditions. The boundary conditions (12) serve to solve the local problems (10) on the dual cells for the correction functions at step n. Then the nodal pressures p_k are obtained through the solution of a coarse grid system (Hajibeygi, Bonfigli, Hesse, and Jenny, 2008) and a new pressure field $\widetilde{p}^{(n+1)}$ is constructed via

$$\widetilde{p}^{l(n+1)} = \sum_{i=1}^{4} p_i^l \phi_i^l + p_c^l \ \text{ in } \ \widetilde{\Omega}^l. \tag{13}$$

Again, we smooth $\widetilde{p}^{(n+1)}$ to yield a new smoothed field $\widetilde{p}_s^{(n+1)}$ and repeat the iteration until convergence. It was shown by a series of examples in (Hajibeygi, Bonfigli, Hesse, and Jenny, 2008) that this iterative MSFV (iMSFV) method converges to the fine scale reference solution p_f.

The iMSFV method relatively maintains the efficiency of MSFV method and has the possibility to approach the accuracy of corresponding fine scale solver. This method has been successfully applied to incompressible (Hajibeygi, Bonfigli, Hesse, and Jenny, 2008) and compressible (Hajibeygi and Jenny, 2009) multiphase flow in porous media. Recently, it is used adaptively (Hajibeygi and Jenny, 2011) and extended to simulate multiphase flow in fractured porous media (Hajibeygi, Karvounis, and Jenny, 2011).

5 Proposed RBF-based multiscale control-volume method

In this work we are interested in a one-parameter (ε) form of the multiscale elliptic problem (1), i.e.

$$-\nabla \cdot (\mathbf{a}^\varepsilon(\mathbf{x}) \nabla u(\mathbf{x})) = f(\mathbf{x}) \ \text{ in } \ \Omega \tag{14}$$

with the boundary conditions $\nabla u \cdot \mathbf{n} = b$ and $u(\mathbf{x}) = g$ on $\partial \Omega_1$ and $\partial \Omega_2$, respectively. Note that $\partial \Omega = \partial \Omega_1 \cup \partial \Omega_2$ and $\mathbf{n}$ is the outward unit vector normal to $\partial \Omega$. $\mathbf{a}^\varepsilon$ is the coefficient tensor which is positive-definite with upper and lower bounds and involving a small scale ε, and f, b and g are specified fields. This elliptic problem usually arises in modeling composite materials and porous media flows. In the case

of heat conduction in composite materials, *u* and **a** represent the temperature and thermal conductivity, respectively. In the case of flows in porous media, *u* is the pressure and **a** is the mobility field.

For the reasons mentioned above, the MFEM is an efficient method to capture the large scale solution but cannot produce the fine scale reference solution. In addition, the method used in MFEM to determine the basis functions and solve the global coarse mesh problem is a linear finite element formulation. Note that there is an attempt to use a high-order method, e.g. the Chebyshev spectral method, to determine the basis functions in Hou and Wu (1997); Hou, Wu, and Cai (1999). They found that the accuracy of the final results is relatively insensitive to the accuracy of the basis functions. On the other hand, as described above, though possessing conservative property the MSFV method strongly resemble the MFEM and hence also cannot produce the fine scale reference solution. In contrast to the MFEM and the MSFV method, the iMSFV method (Hajibeygi, Bonfigli, Hesse, and Jenny, 2008) can produce the reference solution efficiently. However, a low order smoother has been used which results in a low-order accuracy relative to the exact solution. Moreover, like the MSFV method the iMSFV method requires a further reconstruction step to obtain a continuous velocity field for the solution of transport equations. It is pointed out in (Chen and Hou, 2002) that this is a compulsory step to accurately solve the flow-transport-related applications, e.g. the single and multiphase flows through porous media.

It is desirable to develop a multiscale computational framework which can produce the fine scale reference solution of elliptic problem (14) with high efficiency and accuracy. In the following, we propose a high-order conservative multiscale computational framework based on 2-node IRBFEs for solving (14). Unlike other multiscale computational frameworks, the proposed method can produce fine scale reference solutions efficiently with high accuracy. Furthermore, iterative solutions which converge to C^2-continuous reference solutions are obtained in 2D problems. As a result, intrinsically continuous velocity fields are guaranteed automatically in flow-transport-related applications without the need for a reconstruction step. Because of fundamental differences, the proposed method for 1D and 2D problems is presented independently, following a brief review of the two-node integrated-RBF elements in our discretisation scheme based on Cartesian grids.

5.1   *Two-node integrated-RBF elements (IRBFEs)*

Assume that a Cartesian grid is used to discretise a rectangular domain Ω. As a result, a set of nodal points includes interior grid nodes and boundary nodes which are defined as the intersection of the grid lines and the boundaries. Over straight-line segments between two adjacent nodal points, 1D-IRBFs (e.g. Mai-Duy and

10

Tanner (2007)) are utilised to represent the variation of the field variable and its derivatives, forming 2-node IRBFEs. It can be seen that there are two types of elements, namely interior and semi-interior elements. An interior element is formed using two adjacent interior nodes while a semi-interior element is generated by an interior node and a boundary node (Fig. 3).

5.1.1 Interior elements

1D-IRBF expressions for interior elements are of similar forms. Consider an interior element, $\eta \in [\eta_1, \eta_2]$, and its two nodes are locally named as 1 and 2. Let $\phi(\eta)$ be a function and ϕ_1, $\partial \phi_1 / \partial \eta$, ϕ_2 and $\partial \phi_2 / \partial \eta$ be the values of ϕ and $\partial \phi / \partial \eta$ at the two nodes, respectively (Fig. 4(a)). The 2-node IRBFE scheme approximates the second-order derivative of $\phi(\eta)$ using two multiquadric (MQ) functions whose centres are located at η_1 and η_2

$$\frac{\partial^2 \phi}{\partial \eta^2}(\eta) = w_1 \sqrt{(\eta - \eta_1)^2 + a_1^2} + w_2 \sqrt{(\eta - \eta_2)^2 + a_2^2} = w_1 I_1^{(2)}(\eta) + w_2 I_2^{(2)}(\eta),$$
(15)

where $I_i^{(2)}(\eta)$ conveniently denotes the MQ, w_i and a_i are the associated weight and MQ-width at node i ($i \in \{1, 2\}$). We simply take $a_i = \beta h$, where h is a grid size and β is a factor.

First-order derivative of ϕ and the function ϕ are approximated by integrating (15) with respect to η

$$\frac{\partial \phi}{\partial \eta}(\eta) = w_1 I_1^{(1)}(\eta) + w_2 I_2^{(1)}(\eta) + C_1,$$
(16)

$$\phi(\eta) = w_1 I_1^{(0)}(\eta) + w_2 I_2^{(0)}(\eta) + C_1 \eta + C_2,$$
(17)

where $I_i^{(1)}(\eta) = \int I_i^{(2)}(\eta) d\eta$, $I_i^{(0)}(\eta) = \int I_i^{(1)}(\eta) d\eta$, and C_1 and C_2 are the constants of integration. By collocating (17) and (16) at η_1 and η_2, the relation between the physical space and the RBF coefficient space is obtained

$$\underbrace{\begin{pmatrix} \phi_1 \\ \phi_2 \\ \frac{\partial \phi_1}{\partial \eta} \\ \frac{\partial \phi_2}{\partial \eta} \end{pmatrix}}_{\widehat{\phi}} = \underbrace{\begin{pmatrix} I_1^{(0)}(\eta_1) & I_2^{(0)}(\eta_1) & \eta_1 & 1 \\ I_1^{(0)}(\eta_2) & I_2^{(0)}(\eta_2) & \eta_2 & 1 \\ I_1^{(1)}(\eta_1) & I_2^{(1)}(\eta_1) & 1 & 0 \\ I_1^{(1)}(\eta_2) & I_2^{(1)}(\eta_2) & 1 & 0 \end{pmatrix}}_{\mathscr{I}} \underbrace{\begin{pmatrix} w_1 \\ w_2 \\ C_1 \\ C_2 \end{pmatrix}}_{\widehat{w}},$$
(18)

where $\widehat{\phi}$ is the nodal-value vector, $\mathscr{I}$ the conversion matrix, and $\widehat{w}$ the coefficient vector. It is noted that not only the nodal values of ϕ but also of $\partial \phi / \partial \eta$ are incorporated into the conversion system and this imposition is done in an exact manner

owing to the presence of integration constants. Solving (18) yields

$$\widehat{w} = \mathscr{I}^{-1}\widehat{\phi}. \tag{19}$$

Substitution of (19) into (17), (16) and (15) leads to

$$\phi(\eta) = \left[I_1^{(0)}(\eta), I_2^{(0)}(\eta), \eta, 1 \right] \mathscr{I}^{-1}\widehat{\phi}, \tag{20}$$

$$\frac{\partial \phi}{\partial \eta}(\eta) = \left[I_1^{(1)}(\eta), I_2^{(1)}(\eta), 1, 0 \right] \mathscr{I}^{-1}\widehat{\phi}, \tag{21}$$

$$\frac{\partial^2 \phi}{\partial \eta^2}(\eta) = \left[I_1^{(2)}(\eta), I_2^{(2)}(\eta), 0, 0 \right] \mathscr{I}^{-1}\widehat{\phi}. \tag{22}$$

They can be rewritten in the form

$$\phi(\eta) = \varphi_1(\eta)\phi_1 + \varphi_2(\eta)\phi_2 + \varphi_3(\eta)\frac{\partial \phi_1}{\partial \eta} + \varphi_4(\eta)\frac{\partial \phi_2}{\partial \eta}, \tag{23}$$

$$\frac{\partial \phi}{\partial \eta}(\eta) = \frac{\partial \varphi_1(\eta)}{\partial \eta}\phi_1 + \frac{\partial \varphi_2(\eta)}{\partial \eta}\phi_2 + \frac{\partial \varphi_3(\eta)}{\partial \eta}\frac{\partial \phi_1}{\partial \eta} + \frac{\partial \varphi_4(\eta)}{\partial \eta}\frac{\partial \phi_2}{\partial \eta}, \tag{24}$$

$$\frac{\partial^2 \phi}{\partial \eta^2}(\eta) = \frac{\partial^2 \varphi_1(\eta)}{\partial \eta^2}\phi_1 + \frac{\partial^2 \varphi_2(\eta)}{\partial \eta^2}\phi_2 + \frac{\partial^2 \varphi_3(\eta)}{\partial \eta^2}\frac{\partial \phi_1}{\partial \eta} + \frac{\partial^2 \varphi_4(\eta)}{\partial \eta^2}\frac{\partial \phi_2}{\partial \eta}, \tag{25}$$

where $\{\varphi_i(\eta)\}_{i=1}^4$ is the set of basis functions in the physical space. These expressions allow one to compute the values of ϕ, $\partial \phi/\partial \eta$, and $\partial^2 \phi/\partial \eta^2$ at any point η in $[\eta_1, \eta_2]$ in terms of four nodal unknowns, i.e. the values of the field variable and its first-order derivatives at the two extremes (also grid points) of the element.

For convenience, in the case of $\eta \equiv x$, we denote

$$\mu_i = \frac{\partial \varphi_i}{\partial x}\left(\frac{x_1 + x_2}{2}\right), \tag{26}$$

$$\nu_i = \frac{\partial^2 \varphi_i}{\partial x^2}(x_1), \tag{27}$$

$$\zeta_i = \frac{\partial^2 \varphi_i}{\partial x^2}(x_2), \tag{28}$$

and in the case of $\eta \equiv y$,

$$\theta_i = \frac{\partial \varphi_i}{\partial y}\left(\frac{y_1 + y_2}{2}\right), \tag{29}$$

$$\vartheta_i = \frac{\partial^2 \varphi_i}{\partial y^2}(y_1), \tag{30}$$

$$\xi_i = \frac{\partial^2 \varphi_i}{\partial y^2}(y_2), \tag{31}$$

where $\quad i \in \{1, 2, 3, 4\}$.

12

5.1.2 Semi-interior elements

As mentioned earlier, a semi-interior element is defined by two nodes: an interior node and a boundary node. The subscripts 1 and 2 are now replaced with b (for a boundary node) and g (for an interior grid node), respectively (Fig. 4(b)). Assume that the value of ϕ is given at η_b. The conversion system can be formed as

$$\begin{pmatrix} \phi_b \\ \phi_g \\ \frac{\partial \phi_g}{\partial \eta} \end{pmatrix} = \begin{pmatrix} I_b^{(0)}(\eta_b) & I_g^{(0)}(\eta_b) & \eta_b & 1 \\ I_b^{(0)}(\eta_g) & I_g^{(0)}(\eta_g) & \eta_g & 1 \\ I_b^{(1)}(\eta_g) & I_g^{(1)}(\eta_g) & 1 & 0 \end{pmatrix} \begin{pmatrix} w_b \\ w_g \\ C_1 \\ C_2 \end{pmatrix}, \tag{32}$$

which leads to

$$\phi(\eta) = \varphi_1(\eta)\phi_b + \varphi_2(\eta)\phi_g + \varphi_3(\eta)\frac{\partial \phi_g}{\partial \eta}, \tag{33}$$

$$\frac{\partial \phi}{\partial \eta}(\eta) = \frac{\partial \varphi_1(\eta)}{\partial \eta}\phi_b + \frac{\partial \varphi_2(\eta)}{\partial \eta}\phi_g + \frac{\partial \varphi_3(\eta)}{\partial \eta}\frac{\partial \phi_g}{\partial \eta}, \tag{34}$$

$$\frac{\partial^2 \phi}{\partial \eta^2}(\eta) = \frac{\partial^2 \varphi_1(\eta)}{\partial \eta^2}\phi_b + \frac{\partial^2 \varphi_2(\eta)}{\partial \eta^2}\phi_g + \frac{\partial^2 \varphi_3(\eta)}{\partial \eta^2}\frac{\partial \phi_g}{\partial \eta}. \tag{35}$$

It can be seen that the conversion matrix in (32) is under-determined and its inverse can be obtained using the SVD technique (pseudo-inversion). Owing to the facts that point collocation is used and the RBF conversion matrix is not over-determined, the boundary condition ϕ_b is imposed in an exact manner in the sense that the error is due to the numerical inversion only and there is no intrinsic approximation errors such as those associated with "unconstrained" boundary conditions imposed by certain finite element methods (Burnett, 1987). For Neumann boundary conditions such as given surface traction or boundary pressure, other types of semi-interior elements have been proposed in (An-Vo, Mai-Duy, and Tran-Cong, 2011a) to which the reader is referred for details.

5.2 Proposed method for 1D problems

In a 1D domain, problem (14) reduces to

$$-\frac{\mathrm{d}}{\mathrm{d}x}\left(a^{\varepsilon}(x)\frac{\mathrm{d}u(x)}{\mathrm{d}x}\right) = f(x), \ x \in \Omega, \tag{36}$$

where $a^{\varepsilon}(x)$ is a single variable function involving a small scale parameter ε. The problem domain is represented using a set of N nodal points, called a global coarse scale grid. This grid is used to obtain the coarse scale solution of problem (36). On

each interval or coarse cell $\widetilde{\Omega}^l$, $\widetilde{\Omega}^l = [x_{i-1}, x_i]$ with $i \in [2, N]$ and $l \in [1, N-1]$, an approximation to the field variable u is sought in the form

$$u^l(x) = \phi_{i-1}^l(x)u_{i-1} + \phi_i^l(x)u_i + u_c^l(x), \tag{37}$$

where $x \in \widetilde{\Omega}^l$, $u_{i-1} = u(x_{i-1})$, $u_i = u(x_i)$, $\phi_{i-1}^l(x)$ and $\phi_i^l(x)$ are the basis functions associated with the nodes x_{i-1} and x_i respectively on the coarse cell $\widetilde{\Omega}^l$, and $u_c^l(x)$ is the correction function associated with the coarse cell $\widetilde{\Omega}^l$.

We employ subregion collocation to discretise (36). Each node x_i with $i \in [2, N-1]$ is surrounded by a control volume $\overline{\Omega}_i$, $\overline{\Omega}_i = [x_{i-1/2}, x_{i+1/2}]$ as shown in Fig. 5. Integrating (36) over a control volume $\overline{\Omega}_i$, one has

$$a^\varepsilon(x_{i+1/2})\frac{\mathrm{d}u}{\mathrm{d}x}(x_{i+1/2}) - a^\varepsilon(x_{i-1/2})\frac{\mathrm{d}u}{\mathrm{d}x}(x_{i-1/2}) + \int_{x_{i-1/2}}^{x_{i+1/2}} f\mathrm{d}x = 0. \tag{38}$$

Taking (37) into account, one can express first derivatives in (38) in terms of nodal values of u. Unlike traditional discretisation methods, the basis functions $\phi_{i-1}^l(x)$ and $\phi_i^l(x)$ on a coarse cell $\widetilde{\Omega}^l$ are not analytic functions (e.g. not polynomials), but local numerical solutions to the following differential equation

$$\frac{\mathrm{d}}{\mathrm{d}x}\left(a^\varepsilon\frac{\mathrm{d}\phi_k^l}{\mathrm{d}x}\right) = 0 \tag{39}$$

with $k \in \{i-1, i\}$ and $x \in \widetilde{\Omega}^l$. Boundary conditions for (39) are specified using the condition $\phi_k^l(x_j) = \delta_{kj}$ with $j \in \{i-1, i\}$. Likewise, the correction function $u_c^l(x)$ is a numerical solution to the following differential equation

$$-\frac{\mathrm{d}}{\mathrm{d}x}\left(a^\varepsilon\frac{\mathrm{d}u_c^l}{\mathrm{d}x}\right) = f \tag{40}$$

with homogeneous boundary conditions $u_c^l(x_j) = 0$, $j \in \{i-1, i\}$. Unlike (39) the right hand side f of the governing equation (36) is involved in (40). Equation (39) needs to be solved twice while equation (40) needs to be solved once for the determination of the two basis functions and the correction function respectively on each coarse cell. A coarse cell $\widetilde{\Omega}^l$ is discretised by a set of n points, called local fine scale grid. Such a grid is used to capture the fine scale structure information of the solution. Let $\{\eta_1 = x_{i-1}, \eta_2, \ldots, \eta_n = x_i\}$ be a set of nodes of the local fine scale grid. Similar to a coarse scale node, each fine scale node η_m with $m \in [2, n-1]$ is surrounded by a local control volume $\overline{\Omega}_m$, $\overline{\Omega}_m = [\eta_{m-1/2}, \eta_{m+1/2}]$. Integrating (39)

14

and (40) over $\overline{\Omega}_m$, one has respectively

$$a^\varepsilon(\eta_{m+1/2})\frac{\mathrm{d}\phi_k^l}{\mathrm{d}x}(\eta_{m+1/2}) - a^\varepsilon(\eta_{m-1/2})\frac{\mathrm{d}\phi_k^l}{\mathrm{d}x}(\eta_{m-1/2}) = 0, \qquad (41)$$

$$a^\varepsilon(\eta_{m+1/2})\frac{\mathrm{d}u_c^l}{\mathrm{d}x}(\eta_{m+1/2}) - a^\varepsilon(\eta_{m-1/2})\frac{\mathrm{d}u_c^l}{\mathrm{d}x}(\eta_{m-1/2}) + \int_{\eta_{m-1/2}}^{\eta_{m+1/2}} f\mathrm{d}\eta = 0. \qquad (42)$$

We propose to approximate the first-order derivatives in (41) and (42) by a 2-node IRBFE scheme, i.e. equation (24). Assuming that η_{m-1} and η_{m+1} are interior fine scale nodes, we can form two interior 2-node IRBFEs at η_m, i.e. elements $[\eta_{m-1}, \eta_m]$ and $[\eta_m, \eta_{m+1}]$, to the left and right side of η_m respectively. Applying (24) with notation (26) to the element $[\eta_{m-1}, \eta_m]$, one has

$$\frac{\mathrm{d}\phi_k^l}{\mathrm{d}x}(\eta_{m-1/2}) = \mu_1\phi_k^l(\eta_{m-1}) + \mu_2\phi_k^l(\eta_m) + \mu_3\frac{\mathrm{d}\phi_k^l}{\mathrm{d}\eta}(\eta_{m-1}) + \mu_4\frac{\mathrm{d}\phi_k^l}{\mathrm{d}\eta}(\eta_m), \qquad (43)$$

$$\frac{\mathrm{d}u_c^l}{\mathrm{d}x}(\eta_{m-1/2}) = \mu_1 u_c^l(\eta_{m-1}) + \mu_2 u_c^l(\eta_m) + \mu_3\frac{\mathrm{d}u_c^l}{\mathrm{d}\eta}(\eta_{m-1}) + \mu_4\frac{\mathrm{d}u_c^l}{\mathrm{d}\eta}(\eta_m). \qquad (44)$$

Similarly, to the element $[\eta_m, \eta_{m+1}]$, one has

$$\frac{\mathrm{d}\phi_k^l}{\mathrm{d}x}(\eta_{m+1/2}) = \mu_1\phi_k^l(\eta_m) + \mu_2\phi_k^l(\eta_{m+1}) + \mu_3\frac{\mathrm{d}\phi_k^l}{\mathrm{d}\eta}(\eta_m) + \mu_4\frac{\mathrm{d}\phi_k^l}{\mathrm{d}\eta}(\eta_{m+1}), \qquad (45)$$

$$\frac{\mathrm{d}u_c^l}{\mathrm{d}x}(\eta_{m+1/2}) = \mu_1 u_c^l(\eta_m) + \mu_2 u_c^l(\eta_{m+1}) + \mu_3\frac{\mathrm{d}u_c^l}{\mathrm{d}\eta}(\eta_m) + \mu_4\frac{\mathrm{d}u_c^l}{\mathrm{d}\eta}(\eta_{m+1}). \qquad (46)$$

Note that (43)-(46) will be slightly different at the coarse cell boundaries (also the coarse scale nodes) where (34) for semi-interior elements is used instead of (24). Substituting (43) and (45) into (41) yields

$$a^\varepsilon(\eta_{m+1/2})\mu_2\phi_k^l(\eta_{m+1}) + \left[a^\varepsilon(\eta_{m+1/2})\mu_1 - a^\varepsilon(\eta_{m-1/2})\mu_2\right]\phi_k^l(\eta_m)$$

$$- a^\varepsilon(\eta_{m-1/2})\mu_1\phi_k^l(\eta_{m-1}) + a^\varepsilon(\eta_{m+1/2})\mu_4\frac{\mathrm{d}\phi_k^l}{\mathrm{d}\eta}(\eta_{m+1})$$

$$+ \left[a^\varepsilon(\eta_{m+1/2})\mu_3 - a^\varepsilon(\eta_{m-1/2})\mu_4\right]\frac{\mathrm{d}\phi_k^l}{\mathrm{d}\eta}(\eta_m) - a^\varepsilon(\eta_{m-1/2})\mu_3\frac{\mathrm{d}\phi_k^l}{\mathrm{d}\eta}(\eta_{m-1}) = 0.$$

$$(47)$$

It can be seen from (47) that there are two unknowns, namely $\phi_k^l(\eta_m)$ and $\mathrm{d}\phi_k^l/\mathrm{d}\eta(\eta_m)$, associated with each nodal points η_m ($m \in [2, n-1]$). Collection of (47) at all nodal points leads to a system of $n-2$ equations for $2 \times (n-2)$ unknowns. For the algebraic system to be solvable one more equation needs to be added at each and every

nodal points η_m, which is here achieved by imposing C^2-continuous condition at η_m, i.e.

$$\left[\frac{\mathrm{d}^2\phi_k^l}{\mathrm{d}\eta^2}(\eta_m)\right]_L = \left[\frac{\mathrm{d}^2\phi_k^l}{\mathrm{d}\eta^2}(\eta_m)\right]_R, \tag{48}$$

where $(.)_L$ indicates that the computation of $(.)$ is based on the element to the left of η_m, i.e. element $[\eta_{m-1}, \eta_m]$, and similarly subscript R denotes the right element $[\eta_m, \eta_{m+1}]$. The left and the right of equation (48) are obtained via expression (25), noting (28) and (27) respectively, yielding

$$\zeta_1 \phi_k^l(\eta_{m-1}) + \zeta_2 \phi_k^l(\eta_m) + \zeta_3 \frac{\mathrm{d}\phi_k^l}{\mathrm{d}\eta}(\eta_{m-1}) + \zeta_4 \frac{\mathrm{d}\phi_k^l}{\mathrm{d}\eta}(\eta_m) =$$
$$v_1 \phi_k^l(\eta_m) + v_2 \phi_k^l(\eta_{m+1}) + v_3 \frac{\mathrm{d}\phi_k^l}{\mathrm{d}\eta}(\eta_m) + v_4 \frac{\mathrm{d}\phi_k^l}{\mathrm{d}\eta}(\eta_{m+1}). \tag{49}$$

Collection of equations (47) and (49) at each and every fine scale nodes η_m ($m \in [2, n-1]$) with the associated boundary conditions leads to two systems of $2 \times (n-2)$ equations for $2 \times (n-2)$ unknowns. These two systems are solved for the two basis functions on $\widetilde{\Omega}^l$. Unlike other conventional discretisation techniques, both the field variable and its first-derivative are considered in the present proposed technique, resulting C^2-continuous solutions for the basis functions.

Similarly, at each fine scale node η_m, substituting (44) and (46) into (42) and imposing C^2-continuous condition at η_m lead to two equations for two unknowns associated with η_m. Collection of these equations at all fine scale nodes with the homogeneous boundary conditions results in a system of $2 \times (n-1)$ equations for $2 \times (n-1)$ unknowns. This system is solved for the correction function u_c^l associated with the coarse cell $\widetilde{\Omega}^l$.

The set of basis and correction functions of the whole domain Ω is used to represent the first derivatives in (38) in terms of coarse scale nodal values u_i ($i \in [2, N-1]$). Collection of equation (38) at all coarse scale nodes with the associated boundary conditions lead to a coarse scale system of $N-2$ equations for $N-2$ coarse scale nodal values of u. Consequently, the complete solution of problem (36) is constructed on each and every coarse cell $\widetilde{\Omega}^l$ via (37). It can be seen that the presently proposed multiscale method is conservative for both local and global problems.

5.3 *Proposed method for 2D problems*

We consider the coefficient tensor $\mathbf{a}^\varepsilon$ in the following form

$$\mathbf{a}^\varepsilon = \begin{pmatrix} a^\varepsilon(x) & 0 \\ 0 & b^\varepsilon(y) \end{pmatrix}, \tag{50}$$

16

where $a^\varepsilon(x)$ and $b^\varepsilon(y)$ are oscillatory functions involving a small scale ε. It is noted that the periodicity and scale separation assumptions of $a^\varepsilon(x)$ and $b^\varepsilon(y)$ are not necessary here. The two-dimensional equation (14) becomes

$$-\frac{\partial}{\partial x}\left(a^\varepsilon(x)\frac{\partial u}{\partial x}\right) - \frac{\partial}{\partial y}\left(b^\varepsilon(y)\frac{\partial u}{\partial y}\right) = f(x,y). \tag{51}$$

Here we are considering a particular class (51) of the general problem (14) for the convenience of presenting the main features of the proposed method. Extension of the proposed method to the general problem where $\mathbf{a}^\varepsilon$ is a full tensor requires consideration of a mixed derivative term and will be reported in an up-coming work. Nevertheless, the multiscale problem (51) does have important application in, e.g. two-dimensional semi-conductor quantum devices wherein there is a specific direction oscillation of the coefficients at each location in space and time. The readers are referred to (Wang and Shu, 2009) for the application of such device models in one-dimension.

A Cartesian grid system is employed to represent the problem domain Ω in a manner similar to that in the MSFV method (e.g. Fig. 1). Integrating (51) over a control volume $\overline{\Omega}_k$ and then applying the Green's theorem in plane, one has

$$-\int_{\overline{\Omega}_k}\left[\frac{\partial}{\partial x}\left(a^\varepsilon(x)\frac{\partial u}{\partial x}\right) + \frac{\partial}{\partial y}\left(b^\varepsilon(y)\frac{\partial u}{\partial y}\right)\right]d\Omega =$$
$$-\int_{\partial\overline{\Omega}_k}a^\varepsilon(x)\frac{\partial u}{\partial x}dy + \int_{\partial\overline{\Omega}_k}b^\varepsilon(y)\frac{\partial u}{\partial y}dx = A_k f_k, \quad (52)$$

where A_k is the area of $\overline{\Omega}_k$ and

$$f_k = \frac{1}{A_k}\int_{\overline{\Omega}_k}f d\Omega. \tag{53}$$

Approximating the line integrals in (52) by the midpoint rule, one obtains

$$-\left[\left(a^\varepsilon(x)\frac{\partial u}{\partial x}\right)_e - \left(a^\varepsilon(x)\frac{\partial u}{\partial x}\right)_w\right]\Delta_y - \left[\left(b^\varepsilon(y)\frac{\partial u}{\partial y}\right)_n - \left(b^\varepsilon(y)\frac{\partial u}{\partial y}\right)_s\right]\Delta_x = A_k f_k,$$
$$(54)$$

where Δ_x and Δ_y are the coarse grid spacing in x and y direction respectively; and the subscripts e, w, n and s are used to indicate that the flux is estimated at the intersections of the dual grid lines with the east, west, north and south faces of the control volume $\overline{\Omega}_k$, respectively (Fig. 2).

To estimate the first-order derivatives of u in (54) we consider the dual coarse cells $\widetilde{\Omega}^l$ in a 2D computational domain as shown in Fig. 1. We seek the approximation for the field variable u on each $\widetilde{\Omega}^l$ in the form

$$u^l(\mathbf{x}) = \sum_{i=1}^{4} \phi_i^l(\mathbf{x})u_i + u_c^l(\mathbf{x}), \tag{55}$$

where $\phi_i^l(\mathbf{x})$ is the basis function associated with a coarse scale node $\mathbf{x}_i$ and $i \in [1,4]$ is the local index of the four nodes of a coarse cell $\widetilde{\Omega}^l$, $u_i = u(\mathbf{x}_i)$, and $u_c^l(\mathbf{x})$ is the correction function associated with a coarse cell $\widetilde{\Omega}^l$. As explained earlier via (4) and (10), these basis functions and correction function are similarly local numerical solutions of problem (51) on $\widetilde{\Omega}^l$ without and with right-hand side, respectively, i.e.

$$-\frac{\partial}{\partial x}\left(a^\varepsilon(x)\frac{\partial \phi_i^l}{\partial x}\right) - \frac{\partial}{\partial y}\left(b^\varepsilon(y)\frac{\partial \phi_i^l}{\partial y}\right) = 0, \tag{56}$$

$$-\frac{\partial}{\partial x}\left(a^\varepsilon(x)\frac{\partial u_c^l}{\partial x}\right) - \frac{\partial}{\partial y}\left(b^\varepsilon(y)\frac{\partial u_c^l}{\partial y}\right) = f(x,y). \tag{57}$$

Boundary conditions for (56) are

$$\frac{\partial}{\partial x}\left(a^\varepsilon(x)\frac{\partial \phi_i^l}{\partial x}\right) = 0 \ \text{ on } \ \partial\widetilde{\Omega}_x^l, \tag{58}$$

$$\frac{\partial}{\partial y}\left(b^\varepsilon(y)\frac{\partial \phi_i^l}{\partial y}\right) = 0 \ \text{ on } \ \partial\widetilde{\Omega}_y^l, \tag{59}$$

and for (57) are

$$\frac{\partial}{\partial x}\left(a^\varepsilon(x)\frac{\partial u_c^l}{\partial x}\right) = \frac{\partial}{\partial x}\left(a^\varepsilon(x)\frac{\partial u_f}{\partial x}\right) \ \text{ on } \ \partial\widetilde{\Omega}_x^l, \tag{60}$$

$$\frac{\partial}{\partial y}\left(b^\varepsilon(y)\frac{\partial u_c^l}{\partial y}\right) = \frac{\partial}{\partial y}\left(b^\varepsilon(y)\frac{\partial u_f}{\partial y}\right) \ \text{ on } \ \partial\widetilde{\Omega}_y^l, \tag{61}$$

where $\partial\widetilde{\Omega}_x^l$ and $\partial\widetilde{\Omega}_y^l$ denote the x- and y-segments, respectively, of the boundary of a dual cell $\widetilde{\Omega}^l$ and u_f is a reference solution on the global fine scale grid. A method to create a fine scale reference solution u_f will be presented in the following section. At the dual-grid nodes $\mathbf{x}_i$ which belong to $\widetilde{\Omega}^l$, $\phi_j^l(\mathbf{x}_i) = \delta_{ji}$ ($j \in [1,4]$) and $u_c^l(\mathbf{x}_i) = 0$. Note that outside $\widetilde{\Omega}^l$ the ϕ_j^l and u_c^l are set to zero. In the present approach, a C^2-continuous IRBFE based control volume method (An-Vo, Mai-Duy, and Tran-Cong, 2011a) is used to solve the local problems (56) and (57) with the associated boundary conditions for the basis functions and correction functions respectively.

18

The first-order derivatives of u in (54) can now be estimated by using expressions (55) for u^l in the four dual coarse cells associated with a grid node $\mathbf{x}_k$ (Fig. 2). Specifically, we use local indices of l ($l \in [1,4]$) and i ($i \in [1,9]$) for local dual coarse cells and local coarse nodes, respectively, associated with $\mathbf{x}_k$ and $\mathbf{x}_k \equiv \mathbf{x}_1$ (Fig. 2) to obtain

$$\left(\frac{\partial u}{\partial x}\right)_e = \frac{\partial \phi_1^2}{\partial x}(x_e)u_1 + \frac{\partial \phi_5^2}{\partial x}(x_e)u_5 + \frac{\partial u_c^2}{\partial x}(x_e) = \frac{\partial \phi_1^3}{\partial x}(x_e)u_1 + \frac{\partial \phi_5^3}{\partial x}(x_e)u_5 + \frac{\partial u_c^3}{\partial x}(x_e),$$
$$(62)$$

$$\left(\frac{\partial u}{\partial x}\right)_w = \frac{\partial \phi_9^1}{\partial x}(x_w)u_9 + \frac{\partial \phi_1^1}{\partial x}(x_w)u_1 + \frac{\partial u_c^1}{\partial x}(x_w) = \frac{\partial \phi_9^4}{\partial x}(x_w)u_9 + \frac{\partial \phi_1^4}{\partial x}(x_w)u_1 + \frac{\partial u_c^4}{\partial x}(x_w),$$
$$(63)$$

$$\left(\frac{\partial u}{\partial y}\right)_n = \frac{\partial \phi_1^3}{\partial y}(y_n)u_1 + \frac{\partial \phi_7^3}{\partial y}(y_n)u_7 + \frac{\partial u_c^3}{\partial y}(y_n) = \frac{\partial \phi_1^4}{\partial y}(y_n)u_1 + \frac{\partial \phi_7^4}{\partial y}(y_n)u_7 + \frac{\partial u_c^4}{\partial y}(y_n),$$
$$(64)$$

$$\left(\frac{\partial u}{\partial y}\right)_s = \frac{\partial \phi_3^1}{\partial y}(y_s)u_3 + \frac{\partial \phi_1^1}{\partial y}(y_s)u_1 + \frac{\partial u_c^1}{\partial y}(y_s) = \frac{\partial \phi_3^2}{\partial y}(y_s)u_3 + \frac{\partial \phi_1^2}{\partial y}(y_s)u_1 + \frac{\partial u_c^2}{\partial y}(y_s).$$
$$(65)$$

We substitute (62)-(65) into (54) to obtain the discretised equation at a coarse node $\mathbf{x}_k$. Collection of the discretised equations at all coarse nodes leads to a linear system to be solved for the coarse scale nodal values u_k, $k \in [1, N-2 \times N-2]$. Consequently, the solution for u in each dual coarse cell $\widetilde{\Omega}^l$ is reconstructed via u_k and the approximation (55). By implementing the reconstruction on the whole problem domain Ω, the global solution for u is obtained.

It should be noted that the current computational framework for u depends strongly on the boundary conditions of local problems for the determination of the correction functions, i.e. (60) and (61), which unfortunately require a priori knowledge of u_f. To obtain the fine scale reference solution u_f one typically has to directly resolve all the small scale features of a multiscale problem. In the following section, we avoid this costly and even impossible task by proposing a conservative fine scale solver based on 2-node IRBFEs.

5.3.1 Fine scale C^2-continuous conservative solver

Consider problem (51) on a global fine scale grid. Each fine scale node, similar to a coarse scale node, is surrounded by a control volume. Integrating (51) over the control volume Ω_P of a fine scale interior grid node P (Fig. 6) by a similar

procedure in obtaining (54), one has

$$
-\left[\left(a^{\varepsilon}(x)\frac{\partial u}{\partial x}\right)_e - \left(a^{\varepsilon}(x)\frac{\partial u}{\partial x}\right)_w\right]\delta_y - \left[\left(b^{\varepsilon}(y)\frac{\partial u}{\partial y}\right)_n - \left(b^{\varepsilon}(y)\frac{\partial u}{\partial y}\right)_s\right]\delta_x = A_P f_P,
$$

(66)

where δ_x and δ_y are fine grid spacing in x and y direction respectively; the subscripts e, w, n and s are now used to indicate that the flux is estimated at the intersections of the fine grid lines with the east, west, north and south faces of the control volume Ω_P, respectively (Fig. 6); and A_P is the area of Ω_P and $f_P = \frac{1}{A_P}\int_{\Omega_P} f\mathrm{d}\Omega$. Unlike (62)-(65), the fluxes are presently computed via 2-node IRBFEs defined over line segments between P and its neighbouring grid nodes (E, W, N and S). There are 4 IRBFEs associated with a control volume Ω_P. Assuming that PE, WP are interior elements and making use of (24), noting (26), one obtains fluxes in the x-direction as

$$
\left(\frac{\partial u}{\partial x}\right)_e = \mu_1 u_P + \mu_2 u_E + \mu_3\frac{\partial u_P}{\partial x} + \mu_4\frac{\partial u_E}{\partial x} \text{ with } x_1 \equiv x_P \text{ and } x_2 \equiv x_E,
$$

(67)

$$
\left(\frac{\partial u}{\partial x}\right)_w = \mu_1 u_W + \mu_2 u_P + \mu_3\frac{\partial u_W}{\partial x} + \mu_4\frac{\partial u_P}{\partial x} \text{ with } x_1 \equiv x_W \text{ and } x_2 \equiv x_P.
$$

(68)

Expressions for the flux at the faces $y = y_n$ and $y = y_s$ are of similar forms obtained by using PN and SP, assumed as interior elements, and making use of (24), noting (29),

$$
\left(\frac{\partial u}{\partial y}\right)_n = \theta_1 u_P + \theta_2 u_N + \theta_3\frac{\partial u_P}{\partial y} + \theta_4\frac{\partial u_N}{\partial y} \text{ with } y_1 \equiv y_P \text{ and } y_2 \equiv y_N,
$$

(69)

$$
\left(\frac{\partial u}{\partial y}\right)_s = \theta_1 u_S + \theta_2 u_P + \theta_3\frac{\partial u_S}{\partial y} + \theta_4\frac{\partial u_P}{\partial y} \text{ with } y_1 \equiv y_S \text{ and } y_2 \equiv y_P.
$$

(70)

(67)-(70) may change if PE, WP, PN, and SP are semi-interior elements where (34) is used instead of (24).

Substituting (67)-(70) into (66), one has

$$
G^{[x]}\begin{bmatrix} u_W \\ u_P \\ u_E \end{bmatrix} + G^{[y]}\begin{bmatrix} u_S \\ u_P \\ u_N \end{bmatrix} + D^{[x]}\begin{bmatrix} \frac{\partial u_W}{\partial x} \\ \frac{\partial u_P}{\partial x} \\ \frac{\partial u_E}{\partial x} \end{bmatrix} + D^{[y]}\begin{bmatrix} \frac{\partial u_S}{\partial y} \\ \frac{\partial u_P}{\partial y} \\ \frac{\partial u_N}{\partial y} \end{bmatrix} = A_P f_P,
$$

(71)

20

where

$$G^{[x]} = - \begin{bmatrix} -a^\varepsilon(x_w)\mu_1 & a^\varepsilon(x_e)\mu_1 - a^\varepsilon(x_w)\mu_2 & a^\varepsilon(x_e)\mu_2 \end{bmatrix} \delta_y, \tag{72}$$

$$G^{[y]} = - \begin{bmatrix} -b^\varepsilon(y_s)\theta_1 & b^\varepsilon(y_n)\theta_1 - b^\varepsilon(y_s)\theta_2 & b^\varepsilon(y_n)\theta_2 \end{bmatrix} \delta_x, \tag{73}$$

$$D^{[x]} = - \begin{bmatrix} -a^\varepsilon(x_w)\mu_3 & a^\varepsilon(x_e)\mu_3 - a^\varepsilon(x_w)\mu_4 & a^\varepsilon(x_e)\mu_4 \end{bmatrix} \delta_y, \tag{74}$$

$$D^{[y]} = - \begin{bmatrix} -b^\varepsilon(y_s)\theta_3 & b^\varepsilon(y_n)\theta_3 - b^\varepsilon(y_s)\theta_4 & b^\varepsilon(y_n)\theta_4 \end{bmatrix} \delta_x. \tag{75}$$

It can be seen from (71), there are three unknowns, namely u_P, $\partial u_P/\partial x$ and $\partial u_P/\partial y$, at a grid node P. To solve (71), two additional equations are needed and devised here by enforcing C^2-continuity condition at P in x- and y-directions, i.e.

$$\left(\frac{\partial^2 u_P}{\partial x^2} \right)_L = \left(\frac{\partial^2 u_P}{\partial x^2} \right)_R, \tag{76}$$

$$\left(\frac{\partial^2 u_P}{\partial y^2} \right)_B = \left(\frac{\partial^2 u_P}{\partial y^2} \right)_T, \tag{77}$$

where $(.)_L$ indicates that the computation of $(.)$ is based on the element to the left of P, i.e. element WP, and similarly subscripts R, B, T denote the right (PE), bottom (SP) and top (PN) elements. Making use of (25) with noting (27) and (28) for (76) and (30) and (31) for (77), one has

$$\zeta_1 u_W + \zeta_2 u_P + \zeta_3 \frac{\partial u_W}{\partial x} + \zeta_4 \frac{\partial u_P}{\partial x} = v_1 u_P + v_2 u_E + v_3 \frac{\partial u_P}{\partial x} + v_4 \frac{\partial u_E}{\partial x}, \tag{78}$$

$$\xi_1 u_S + \xi_2 u_P + \xi_3 \frac{\partial u_S}{\partial y} + \xi_4 \frac{\partial u_P}{\partial y} = \vartheta_1 u_P + \vartheta_2 u_N + \vartheta_3 \frac{\partial u_P}{\partial y} + \vartheta_4 \frac{\partial u_N}{\partial y}. \tag{79}$$

In compact forms, (78) and (79) can be rewritten as

$$C^{[x]} \begin{bmatrix} u_W & u_P & u_E & \frac{\partial u_W}{\partial x} & \frac{\partial u_P}{\partial x} & \frac{\partial u_E}{\partial x} \end{bmatrix}^T = 0, \tag{80}$$

$$C^{[y]} \begin{bmatrix} u_S & u_P & u_N & \frac{\partial u_S}{\partial y} & \frac{\partial u_P}{\partial y} & \frac{\partial u_N}{\partial y} \end{bmatrix}^T = 0, \tag{81}$$

with

$$C^{[x]} = \begin{bmatrix} \zeta_1 & \zeta_2 - v_1 & -v_2 & \zeta_3 & \zeta_4 - v_3 & -v_4 \end{bmatrix}, \tag{82}$$

$$C^{[y]} = \begin{bmatrix} \xi_1 & \xi_2 - \vartheta_1 & -\vartheta_2 & \xi_3 & \xi_4 - \vartheta_3 & -\vartheta_4 \end{bmatrix}. \tag{83}$$

Collection of equations (71), (78) and (79) at all interior nodal points of the global

fine grid leads to a global fine scale system,

$$
\begin{bmatrix} \mathbf{G}^{[x]} + \mathbf{G}^{[y]} & \mathbf{D}^{[x]} & \mathbf{D}^{[y]} \end{bmatrix} \begin{bmatrix} \mathbf{u} \\ \mathbf{u}_x \\ \mathbf{u}_y \end{bmatrix} = \mathbf{R}, \tag{84}
$$

$$
\mathbf{C}^{[x]} \begin{bmatrix} \mathbf{u} \\ \mathbf{u}_x \end{bmatrix} = \mathbf{0}, \tag{85}
$$

$$
\mathbf{C}^{[y]} \begin{bmatrix} \mathbf{u} \\ \mathbf{u}_y \end{bmatrix} = \mathbf{0}, \tag{86}
$$

where $\mathbf{G}^{[\bullet]}, \mathbf{D}^{[\bullet]}$ and $\mathbf{C}^{[\bullet]}$ result from the assembly of $G^{[\bullet]}, D^{[\bullet]}$ and $C^{[\bullet]}$ respectively; $\mathbf{u}, \mathbf{u}_x$ and $\mathbf{u}_y$ are global vectors of values of u at all nodal points and its x- and y-partial derivatives at interior grid nodes; and $\mathbf{R}$ collects the right hand side of (71), which results from the application of (71) at fine scale interior grid nodes.

Instead of directly solving the large fine scale system (84)-(86) for the fine scale reference solution u_f, we propose a line-relaxation (LR) scheme to smooth a temporarily guessed approximate fine grid solution. Assuming that $\mathbf{u}^{(t)}$ and $\mathbf{u}_y^{(t)}$ are a temporarily guessed solution, an iterative strategy in two stages for smoothing is proposed as

$$
\begin{bmatrix} \mathbf{G}^{[x]} + \mathrm{diag}(\mathbf{G}^{[y]}) & \mathbf{D}^{[x]} \\ \mathbf{C}^{[x]} & \end{bmatrix} \begin{bmatrix} \mathbf{u} \\ \mathbf{u}_x \end{bmatrix}^{\gamma+1/2} =
$$
$$
\begin{bmatrix} \mathbf{R} - \begin{bmatrix} \mathbf{G}^{[y]} - \mathrm{diag}(\mathbf{G}^{[y]}) & \mathbf{D}^{[y]} \end{bmatrix} \begin{bmatrix} \mathbf{u} \\ \mathbf{u}_y \end{bmatrix}^{\gamma} \\ \mathbf{0} \end{bmatrix}, \quad (87)
$$

$$
\begin{bmatrix} \mathbf{G}^{[y]} + \mathrm{diag}(\mathbf{G}^{[x]}) & \mathbf{D}^{[y]} \\ \mathbf{C}^{[y]} & \end{bmatrix} \begin{bmatrix} \mathbf{u} \\ \mathbf{u}_y \end{bmatrix}^{\gamma+1} =
$$
$$
\begin{bmatrix} \mathbf{R} - \begin{bmatrix} \mathbf{G}^{[x]} - \mathrm{diag}(\mathbf{G}^{[x]}) & \mathbf{D}^{[x]} \end{bmatrix} \begin{bmatrix} \mathbf{u} \\ \mathbf{u}_x \end{bmatrix}^{\gamma+1/2} \\ \mathbf{0} \end{bmatrix}, \quad (88)
$$

where $\begin{bmatrix} \mathbf{u} & \mathbf{u}_x & \mathbf{u}_y \end{bmatrix}^{\gamma}$ is the approximate solution after the γ smoothing step and $\begin{bmatrix} \mathbf{u} & \mathbf{u}_y \end{bmatrix}^0 = \begin{bmatrix} \mathbf{u}^{(t)} & \mathbf{u}_y^{(t)} \end{bmatrix}$, $\mathrm{diag}(\mathbf{G}^{[x]})$ is the diagonal of $\mathbf{G}^{[x]}$. Owing to the fact that 2-node IRBFE flux approximation is used, the linear systems in (87) and (88) are very sparse. Moreover, these systems can be further split into independent linear systems for each grid line, which is an important property for the implementation

of massively parallel computation. Note that the present C^2-continuous IRBFE-LR solver is convergent, but for large problem the rate is extremely slow. In our framework, however, only a few LR-steps are required to smooth the temporarily guessed approximate solution. The smoothed fine grid solution then serve to estimate temporary boundary conditions for correction functions via (60) and (61) instead of the fine scale reference solution u_f. To ensure that these temporary boundary conditions approach the conditions (60) and (61) an iterative algorithm is used. Such an algorithm is presented next.

5.3.2 *Iterative algorithm*

We present here an iterative algorithm to improve the localised boundary conditions of the correction functions. Such boundary conditions do not depend on u_f. Instead of requirements (60) and (61), we employ an iterative improvement

$$\frac{\partial}{\partial x}\left(a^\varepsilon(x)\frac{\partial u_c^{l^{(t)}}}{\partial x}\right) = \frac{\partial}{\partial x}\left(a^\varepsilon(x)\frac{\partial u_s^{(t)}}{\partial x}\right) \quad \text{on } \partial\widetilde{\Omega}_x^l, \tag{89}$$

$$\frac{\partial}{\partial y}\left(b^\varepsilon(y)\frac{\partial u_c^{l^{(t)}}}{\partial y}\right) = \frac{\partial}{\partial y}\left(b^\varepsilon(y)\frac{\partial u_s^{(t)}}{\partial y}\right) \quad \text{on } \partial\widetilde{\Omega}_y^l \ \forall l \in [1,J]. \tag{90}$$

The superscript (t) denotes an iterative step and

$$\left[\begin{array}{ccc} u_s^{(t)} & \frac{\partial u_s^{(t)}}{\partial x} & \frac{\partial u_s^{(t)}}{\partial y} \end{array}\right] = \mathbf{S}^{n_s}\left(\left[\begin{array}{ccc} u^{(t)} & \frac{\partial u^{(t)}}{\partial x} & \frac{\partial u^{(t)}}{\partial y} \end{array}\right]\right) \tag{91}$$

is a smoothed fine scale approximate solution, where $\mathbf{S}$ is the proposed C^2-continuous IRBFE-LR smoothing operator, i.e. (87) and (88), n_s the number of smoothing steps, and

$$\left[\begin{array}{ccc} u^{(t)} & \frac{\partial u^{(t)}}{\partial x} & \frac{\partial u^{(t)}}{\partial y} \end{array}\right]$$

is the temporary solution which is constructed on each dual coarse cell $\widetilde{\Omega}^l$ as

$$u^{l^{(t)}} = \sum_{i=1}^{4} \phi_i^l u_i^{(t)} + u_c^{l^{(t-1)}}, \tag{92}$$

$$\frac{\partial u^{l^{(t)}}}{\partial x} = \sum_{i=1}^{4} \frac{\partial \phi_i^l}{\partial x} u_i^{(t)} + \frac{\partial u_c^{l^{(t-1)}}}{\partial x}, \tag{93}$$

$$\frac{\partial u^{l^{(t)}}}{\partial y} = \sum_{i=1}^{4} \frac{\partial \phi_i^l}{\partial y} u_i^{(t)} + \frac{\partial u_c^{l^{(t-1)}}}{\partial y} \quad \forall l \in [1,J]. \tag{94}$$

Note that the correction functions $u_c^{l^{(t-1)}}$ are obtained based on local boundary conditions (89) and (90) with $u_s^{(t)}$ replaced by $u_s^{(t-1)}$. A pseudocode of the iterative

algorithm is given below.

---

(1) Initialise $\begin{bmatrix} \mathbf{u}^{(t=0)} & \mathbf{u}_x^{(t=0)} & \mathbf{u}_y^{(t=0)} \end{bmatrix}$

(2) $\forall l$, $\forall i$: compute basis functions ϕ_i^l, equations (56) with boundary conditions (58), (59) by a C^2-continuous IRBFE-CV method (An-Vo, Mai-Duy, and Tran-Cong, 2011a)

(3) for $t = 1$ to number of iterations {

    (3i) $\begin{bmatrix} \mathbf{u}_s^{(t-1)} & \mathbf{u}_{x_s}^{(t-1)} & \mathbf{u}_{y_s}^{(t-1)} \end{bmatrix} = \begin{bmatrix} \mathbf{u}^{(t-1)} & \mathbf{u}_x^{(t-1)} & \mathbf{u}_y^{(t-1)} \end{bmatrix}$

    (3ii) for $i = 1$ to n_s {

        $\begin{bmatrix} \mathbf{u}_s^{(t-1)} & \mathbf{u}_{x_s}^{(t-1)} & \mathbf{u}_{y_s}^{(t-1)} \end{bmatrix} = \mathbf{S}\left(\begin{bmatrix} \mathbf{u}_s^{(t-1)} & \mathbf{u}_{x_s}^{(t-1)} & \mathbf{u}_{y_s}^{(t-1)} \end{bmatrix} \right)$; smoothing step

    }

    (3iii) $\forall l$: compute correction functions $u_c^{l\,(t-1)}$; based on $\mathbf{u}_s^{(t-1)}$, equations (57) with boundary conditions (89) and (90) by a C^2-continuous IRBFE-CV method (An-Vo, Mai-Duy, and Tran-Cong, 2011a)

    (3iv) Calculate right hand side of the coarse grid discretised system

    (3v) Solve coarse system

    (3vi) Reconstruct $\begin{bmatrix} \mathbf{u}^{(t)} & \mathbf{u}_x^{(t)} & \mathbf{u}_y^{(t)} \end{bmatrix}$, equations (92)-(94)

    (3vii) Calculate convergence measures (CMs) through

$$CM(\mathbf{u}) = \frac{\| \mathbf{u}^{(t)} - \mathbf{u}_f \|_2}{\| \mathbf{u}_f \|_2}$$

$$CM(\mathbf{u}_x) = \frac{\| \mathbf{u}_x^{(t)} - \mathbf{u}_{x_f} \|_2}{\| \mathbf{u}_{x_f} \|_2}$$

$$CM(\mathbf{u}_y) = \frac{\| \mathbf{u}_y^{(t)} - \mathbf{u}_{y_f} \|_2}{\| \mathbf{u}_{y_f} \|_2}$$

}.

First, the fine scale field is initialised to zero. Then, all basis functions are computed and the right-hand side of equation (51) is integrated over each coarse volume. These steps have to be performed only once and are followed by the main iteration loop. At the beginning of each iteration, n_s smoothing steps are applied and the smoothed fine scale field is employed to compute the correction functions. The right hand side of the coarse linear system for coarse nodal values also includes induced terms from these correction functions. At the end of each iteration, the coarse system is solved and a new fine scale field is reconstructed.

24

5.3.3 Deferred correction of coarse grid fluxes

In the coarse grid flux expressions, namely (62)-(65), there are required first-derivative values of basis functions and correction functions at the control volume faces. The former needs to be computed only once at the preprocessing stage and be fixed throughout the iteration loop. The latter, however, need to be updated at each iteration via the numerical differentiation of correction functions. This differentiation is usually resulted in a considerable numerical error. Here we propose a deferred correction strategy to obtain the coarse grid fluxes accurately without the need of the numerical differentiation of correction functions. Consider an east control volume face at an iteration level t, instead of using (62) we compute the flux value as

$$
\left(\frac{\partial u}{\partial x}\right)_e^{(t)} = \frac{\partial \phi_1^2}{\partial x}(x_e)u_1^{(t)} + \frac{\partial \phi_5^2}{\partial x}(x_e)u_5^{(t)} + \Delta f_e^{(t-1)} = \frac{\partial \phi_1^3}{\partial x}(x_e)u_1^{(t)} + \frac{\partial \phi_5^3}{\partial x}(x_e)u_5^{(t)} + \Delta f_e^{(t-1)},
$$

(95)

where $\Delta f_e^{(t-1)}$ is the correction term at e which is a known value derived from the smoothed fine scale field, i.e.

$$
\begin{aligned}
\Delta f_e^{(t-1)} &= \left(\frac{\partial u}{\partial x}\right)_e^{(t-1)} - \left(\frac{\partial \phi_1^2}{\partial x}(x_e)u_1^{(t-1)} + \frac{\partial \phi_5^2}{\partial x}(x_e)u_5^{(t-1)}\right) \\
&= \left(\frac{\partial u}{\partial x}\right)_e^{(t-1)} - \left(\frac{\partial \phi_1^3}{\partial x}(x_e)u_1^{(t-1)} + \frac{\partial \phi_5^3}{\partial x}(x_e)u_5^{(t-1)}\right).
\end{aligned}
$$

(96)

Since the proposed C^2-continuous fine scale solver is used the smoothed fine scale field includes not only the field variable but also its first partial derivatives. As a result, the value $(\partial u/\partial x)_e^{(t-1)}$ is explicitly given without the need of numerical differentiation. The flux values at other control-volume faces can be computed in a similar manner. It can be seen that via this correction strategy the coarse grid fluxes are matched with the fine scale smoothed field.

6 Numerical results

The proposed method is verified by solving several problems in one and two dimension. We refer to the size of a coarse grid as N in 1D problems and $N \times N$ in 2D problems and the size of a fine grid on a coarse cell as n and $n \times n$ in 1D and 2D respectively. The fine grid on a coarse cell also referred to as the local fine grid. The fine grid on the whole problem domain is called the global fine grid. In 2D problems, the smoothing system is constructed on the global fine grid. The coarse grid spacing is denoted as H which is also the size of a coarse cell in this study. The

local fine grids on the coarse cells are mapped to $[0,1]$ in 1D problems and $[0,1]^2$ in 2D problems and the grid spacing is denoted as h.

In each problem, two grid refinement strategies are employed. The first strategy, Strategy 1, keeps the coarse grid fixed while refining the local fine grids. In contrast, the second strategy, Strategy 2, keeps the local fine grids fixed while refining the coarse grid. The numerical results are compared with those obtained by the MFEM (Hou, Wu, and Cai, 1999).

The factor of the MQ-width is chosen as $\beta = 15$ throughout the computation. We assess the numerical performance of the proposed method through two measures: (i) the relative discrete L_2 error defined as

$$Ne(\alpha) = \frac{\sqrt{\Sigma_{i=1}^{M}\left(\alpha_i - \alpha_i^{(e)}\right)^2}}{\sqrt{\Sigma_{i=1}^{M}\left(\alpha_i^{(e)}\right)^2}} \tag{97}$$

where M is the number of test points, α denotes the field variable u and its derivatives and (ii) the convergence rates γ with respect to the two grid refinement strategies defined via the error norm behaviours $O(h^\gamma)$ and $O(H^\gamma)$ for the Strategy 1 and 2 respectively. The convergence rates are calculated over 2 successive grids (point-wise rate) and also over the whole set of grids used (average rate).

6.1 One-dimensional examples

6.1.1 Example 1

Consider a model 1D problem (36) with

$$a^\varepsilon(x) = \frac{1}{2 + x + \sin(2\pi x/\varepsilon)}, \quad f = x, \quad \Omega = [0,1], \tag{98}$$

and homogeneous Dirichlet boundary conditions $u(0) = u(1) = 0$.

The problem domain is discretised using a series of uniform coarse elements and the shape functions and correction functions that capture the fine scale physics in the coarse elements are numerically obtained by our C^2-continuous IRBFE-Control Volume (IRBFE-CV) method. Figure 7 shows the basis functions and correction function associated with a typical coarse element. Unlike conventional basis functions, the present basis functions are highly oscillatory since they adapt to the small scale information within each element (Figure 7(a)). The correction function is also highly oscillatory and its scale is small as shown in Figure 7(b). Figure 8 displays the convergence behaviour of a numerical shape function on a typical coarse element obtained by our IRBFE-CVM and the linear FEM. IRBFE-CVM and linear

26

FEM give convergence rates of 4.0267 and 2.0253 respectively. It can be seen that the use of high order approximants in the form of IRBFEs thus helps capture the fine scale physics and hence produce highly accurate solutions.

The coarse scale solution at the coarse grid points is obtained by a conservative CV method where the fluxes are estimated by the obtained shape and correction functions. In order to have a good consistent measure of accuracy, error norms in all cases are computed using the same 10,001 test points where the fine scale solution is recovered via (37). Table 1 presents convergence behaviour associated with Strategy 1 where a fixed coarse scale grid of 10 elements and a series of $21, 41, \dots, 181$ local fine grids are used. The present method converges monotonically while MFEM does not converge. It was pointed out in (Hou and Wu, 1997; Hou, Wu, and Cai, 1999) that the accuracy of the shape functions does not have much effect on the overall accuracy of MFEM. The present approach achieves convergence rates of 3.91, 3.16, and 2.09 for the field variable, its first, and second derivatives respectively. In comparison to multiscale discontinuous Galerkin method proposed by Wang, Guzman, and Shu (2011), in terms of L_2 error, the present method yields two orders of magnitude improvement for the field variable and one order of magnitude improvement for the first derivative by using a local fine grid of $n = 181$. Note that exact shape functions have been used in (Wang, Guzman, and Shu, 2011). Table 2 presents convergence behaviour associated with Strategy 2 where a fixed local fine grid of 27 nodes and a series of $10, 20, \dots, 100$ uniform coarse elements (i.e. $11, 21, \dots, 101$ nodes) are used. Both the present method and the MFEM converge well with refinement of the coarse grids. The present approach achieves convergence rates of 3.03, 2.51, and 1.47 for the field variable, its first, and second derivatives respectively while the MFEM achieves a value of 1.61 for the field variable. These results show superior performance of the present approach indicated by (i) high rates of convergence not only for the field variable but also for the first and second derivatives; (ii) working for both grid refinement strategies. One can thus either keep fine scale or coarse scale grid fixed and obtain convergence by refining the other scale grid.

Figures 9 displays the recovered fine scale results for the field variable $u(x)$ and its first derivative by the present method, MFEM and exact solution. It can be seen that the present method has captured the exact solution much better than MFEM. In addition, the present method can produce approximation of derivatives up to second order as shown in Figure 10.

6.1.2 *Example 2*

In this example, we consider a model 1D problem with highly oscillatory solution at both macro- and micro-scales. The multiscale problem (36) is specifically defined

with

$$a^\varepsilon(x) = \frac{1}{2 + x + \sin(10\pi x/\varepsilon)}, \quad f = 300\sin(10\pi x), \quad \Omega = [0,1], \tag{99}$$

and homogeneous Dirichlet boundary conditions $u(0) = u(1) = 0$.

Similar to example 1, two strategies of grid refinement are implemented here. Table 3 presents the convergence behaviour associated with Strategy 1 where a fixed coarse scale grid of 50 elements and a series of $21, 41, \ldots, 281$ local fine grids are used. Present method converges monotonically as in the case of example 1. The convergence rates are 3.91, 3.24, and 2.13 for the field variable, its first, and second derivatives respectively. Table 4 presents convergence behaviour associated with Strategy 2 where fixed local fine grids of 101 nodes and a series of $10, 20, \ldots, 100$ uniform coarse elements (i.e. $11, 21, \ldots, 101$ nodes) are used. The present method converges well with refinement of the coarse grids. The convergence rates are 3.71, 2.55, and 1.49 for the field variable, its first, and second derivatives respectively.

Figure 11 displays the recovered fine scale solution for the field variable $u(x)$, its first, and second derivatives by the present method and the exact solution. The solutions by the present method are in excellent agreement with the exact solution.

6.2 Two-dimensional examples

We demonstrate that the proposed iterative algorithm for 2D problems converges to the fine scale reference solution. In the following discussion, by "smoother" we mean one iteration of the fine scale solver. By "the present method" we mean a two-grid method where the smoother is invoked for only a few cycles within the iterative algorithm. Computational efficiency of the present method is assessed via a convergence acceleration in comparison with the fine scale solver. The acceleration is estimated by comparing the computational time to achieve a certain convergence measure (*CM*).

6.2.1 Example 1

We consider a special case of equation (51) with $a^\varepsilon(x) = b^\varepsilon(y) = 1$ as follows.

$$\frac{\partial^2 u}{\partial x^2} + \frac{\partial^2 u}{\partial y^2} = -2\pi^2 \cos(\pi x)\cos(\pi y), \tag{100}$$

28

on a square domain $0 \leq x, y \leq 1$ with boundary conditions:

$$u = \cos(\pi y) \qquad \text{for} \qquad x = 0, \ 0 \leq y \leq 1;$$
$$u = -\cos(\pi y) \qquad \text{for} \qquad x = 1, \ 0 \leq y \leq 1;$$
$$u = \cos(\pi x) \qquad \text{for} \qquad y = 0, \ 0 \leq x \leq 1;$$
$$u = -\cos(\pi x) \qquad \text{for} \qquad y = 1, \ 0 \leq x \leq 1.$$

The exact solution to this problem can be verified to be

$$u^{(e)}(x, y) = \cos(\pi x)\cos(\pi y). \tag{101}$$

It can be seen that the basis functions on each coarse cell are simply those of a linear 2D rectangular element in FEM and the MFEM is identical to the conventional FEM. We also utilise these exact basis functions in the present method. The correction functions are numerically obtained via our C^2-continuous CVM (An-Vo, Mai-Duy, and Tran-Cong, 2011a) with the iteratively improved boundary conditions. Figure 12 shows a typical set of converged correction functions on the problem domain.

Iterative convergence: Figure 13 displays the convergence to the reference solution as a function of iterations and smoothing steps (per iteration), n_s, for two grid systems. The first grid system includes a coarse grid of $N \times N = 5 \times 5$ and local fine grids on each coarse cells of $n \times n = 81 \times 81$. The other grid system includes a coarse grid of $N \times N = 33 \times 33$ and local fine grids of $n \times n = 11 \times 11$. Note that these two grid systems have the same size in terms of the global fine grid of 321×321. It can be seen that for both grid systems the smoothing steps have a significant effect on the convergence behaviours. Increasing n_s helps reduce the iterations. In addition, the present method converges well even with only one smoothing step. This robustness is very useful for large scale problems where one smoothing step could require a significant computational load. The convergence behaviours of the first derivatives are similar to those of the field variable. Comparing between the two grid systems (with the same smoothing operation), the use of a larger coarse grid helps reduce the iterations remarkably. For instance with $n_s = 4$, the first grid system (smaller coarse grid) requires about 200 iterations to converge to the reference solution while the other grid system (larger coarse grid) requires only about 20 iterations.

Grid refinement convergence: Two grid refinement strategies are presented in Table 5. In Strategy 1, a fixed coarse grid of $N \times N = 5 \times 5$ is used while the local fine grids on coarse cells $n \times n$ are refined in a series of $11 \times 11, 21 \times 21, \ldots, 91 \times 91$. In contrast, Strategy 2 utilises a series of refined coarse grids of $N \times N = 5 \times 5, 9 \times 9, \ldots, 37 \times 37$ while keeping the size of local fine grids on coarse cells fixed as

$n \times n = 11 \times 11$. The present method converges well with both grid refinement strategies while the MFEM does not converge with Strategy 1. Note that exact basis functions are employed in both MFEM and the present method. The convergence rates of the present method are 1.90 and 1.94 for the field variable and its first derivatives respectively in Strategy 1. A high convergence rate of 4.01 for the field variable is obtained with Strategy 2 where the convergence rate of the MFEM is 2.00.

Solution accuracy: Table 5 also presents the L_2 error norm of the present method in comparison with those of MFEM. Very high levels of accuracy are obtained in the present method. With a small grid system, i.e. $N \times N = 5 \times 5$ and $n \times n = 11 \times 11$, the error is 1.73×10^{-5} and with a relatively larger grid system, i.e. $N \times N = 37 \times 37$ and $n \times n = 11 \times 11$, the error is 2.63×10^{-9}. Compared to the errors of the MFEM, with the same grid systems, the present errors are 3 and 5 orders of magnitude better respectively.

6.2.2 Example 2

Consider a multiscale elliptic problem on a domain $\Omega = [-1,1]^2$ governed by

$$-\frac{\partial}{\partial x}\left(a^\varepsilon(x)\frac{\partial u}{\partial x}\right) - \frac{\partial}{\partial y}\left(b^\varepsilon(y)\frac{\partial u}{\partial y}\right) = xu^e(y) + yu^e(x) \tag{102}$$

with homogeneous Dirichlet boundary condition, where

$$a^\varepsilon(x) = \frac{1}{4 + x + \sin\left(\frac{x}{\varepsilon}\right)}, \quad b^\varepsilon(y) = \frac{1}{4 + y + \sin\left(\frac{y}{\varepsilon}\right)}, \tag{103}$$

and $u^e(x)$ is the exact solution of the one-dimensional problem $-\mathrm{d}(a^\varepsilon(x)\mathrm{d}u/\mathrm{d}x)/\mathrm{d}x = x$ with $a^\varepsilon(x)$ as in (103) (note that $b^\varepsilon(x) = a^\varepsilon(x)$). The exact solution of (102) has the form

$$u(x,y) = u^e(x)u^e(y). \tag{104}$$

Both the basis and correction functions are numerically obtained by our C^2-continuous CVM (An-Vo, Mai-Duy, and Tran-Cong, 2011a) in the present method. The basis functions in MFEM are obtained by a linear FEM. Figure 14 shows typical basis and correction functions in the present method for two cases of small scale parameter, i.e. $\varepsilon = 0.1$ and $\varepsilon = 0.01$. Typical sets of correction functions on the problem domain for these two values of small scale parameter are displayed by contour plots in Figure 15.

Iterative convergence: Figures 16 and 17 display the convergence to the reference solution of the present method in cases of $\varepsilon = 0.1$ and $\varepsilon = 0.01$ respectively. Two

grid systems are employed to study the effect of smoothing steps n_s on the convergence behaviours in each case of ε values. As in example 1, the smoothing steps have a significant effect on the convergence behaviours and we can reduce the number of iterations by increasing n_s. With the same smoothing systems, i.e. 241×241 in the case of $\varepsilon = 0.1$ in Figure 16 and 701×701 in the case of $\varepsilon = 0.01$ in Figure 17, the use of larger coarse grids reduces the iterations remarkably. Computational efficiency is assessed in Figure 18 where the convergence behaviours of the present method ($n_s = 1$) and the fine scale solver (FSS) are presented. It can be seen in Figure 18(a) that the FSS requires about 3.4×10^4 cycles to converge to $CM = 10^{-8}$ in the case of grid 1. By using the smoothing system of grid 1 and with a coarse grid of 5×5 the present method converges to $CM = 10^{-8}$ after about 330 iterations (Figure 18(b)). The number of iterations can reduce to about 42 when a coarse grid of 25×25 is used as shown in Figure 16(b). By using this 25×25 coarse grid, the computational time of each iteration is measured to be 5.24 s on average which include the time of a smoothing cycle, for obtaining correction functions, and for solving the coarse grid system. The computational time of a smoothing cycle is measured to be 4.31 s. It can be seen that the time of a smoothing cycle dominates the time of an iteration. The present method hence has the potential of roughly 1000 times more efficient than the FSS. Furthermore, when we increase the size of the global fine grid to grid 2 and grid 3, the number of cycles of the smoother increases very fast compared to that of the present method (Figure 18(a)).

Grid refinement convergence: The two grid refinement strategies for $\varepsilon = 0.1$ and $\varepsilon = 0.01$ are presented in Tables 6 and 7 respectively. For $\varepsilon = 0.1$, Strategy 1 uses a fixed coarse grid of 5×5 and a series of refined local fine grids of $11 \times 11, 21 \times 21, \ldots, 91 \times 91$. Strategy 2 uses fixed local fine grids of 11×11 and a series of refined coarse grids of $5 \times 5, 9 \times 9, \ldots, 37 \times 37$. The convergence rates of the present method are 3.24 and 3.05 for the field variable and its first derivatives respectively in Strategy 1. It can be seen that MFEM does not converge in Strategy 1. In Strategy 2, the convergence rates of the present method are 3.38 and 1.40 for the field variable and its first derivative respectively. MFEM converges at the rate of 1.95 for the field variable.

For $\varepsilon = 0.01$, Strategy 1 uses a fixed coarse grid of 11×11 and a series of refined local fine grids of $11 \times 11, 21 \times 21, \ldots, 71 \times 71$. Strategy 2 uses a fixed local fine grid of 11×11 and a series of refined coarse grids of $11 \times 11, 21 \times 21, \ldots, 71 \times 71$. The convergence rates of the present method are 4.17, 3.94 and 3.95 for u, $\partial u/\partial x$ and $\partial u/\partial y$ respectively in Strategy 1. These rates are especially high compared to the rate of 0.13 for the field variable in MFEM. In Strategy 2, the convergence rates of the present method are 5.12, 3.60 and 3.59 for u, $\partial u/\partial x$ and $\partial u/\partial y$ respectively while MFEM gives a rate of 2.10 for the field variable.

Solution accuracy: Tables 6 and 7 also present the L_2 error norm for $\varepsilon = 0.1$ and $\varepsilon = 0.01$ respectively. For $\varepsilon = 0.1$ and Strategy 1 (Table 6), the present method achieves the errors of 3.90×10^{-8} and 1.67×10^{-7} for the field variable and its first derivatives respectively by using a grid system of $N \times N = 5 \times 5$ and $n \times n = 91 \times 91$. The error for the field variable is 7 orders of magnitude better compared to that of MFEM by using the same grid system. In Strategy 2, the present method achieves the errors of 2.66×10^{-8} and 3.84×10^{-6} for the field variable and its first derivatives respectively by using a grid system of $N \times N = 37 \times 37$ and $n \times n = 11 \times 11$. The error for the field variable is 5 orders of magnitude better compared to that of MFEM by using the same grid system.

For $\varepsilon = 0.01$ and Strategy 1 (Table 7), the present method achieves the errors of 5.73×10^{-6} and 1.17×10^{-5} for the field variable and its first derivatives respectively by using a grid system of $N \times N = 11 \times 11$ and $n \times n = 71 \times 71$. The error for the field variable is 4 orders of magnitude better compared to that of MFEM by using the same grid system. In Strategy 2, the present method achieves the errors of 9.05×10^{-7}, 2.31×10^{-5} and 2.32×10^{-5} for u, $\partial u/\partial x$ and $\partial u/\partial y$ respectively by using a grid system of $N \times N = 71 \times 71$ and $n \times n = 11 \times 11$. The error for the field variable is more than 3 orders of magnitude better compared to that of MFEM by using the same grid system.

Figure 19 displays the contour plots of the solutions obtained by MFEM, present method and the exact one for $\varepsilon = 0.1$ and $\varepsilon = 0.01$. The present result is obtained with $N \times N = 5 \times 5, n \times n = 31 \times 31$ while the MFEM result is obtained with $N \times N = 11 \times 11, n \times n = 31 \times 31$. It can be seen that the solutions of the present method are in excellent agreement with the exact solution.

7 Concluding remarks

A high-order RBF-based multiscale control-volume method has been successfully developed for 1D and 2D multiscale elliptic problems. To assess the performance of the methods, we use two grid refinement strategies, namely (i) fixed coarse grid and various local fine grids, and (ii) fixed local fine grid and various coarse grids. Unlike MFEM, the proposed methods work well for both grid refinement strategies. High rates of convergence and levels of accuracy are obtained. The method for 2D problems is proposed with an iterative algorithm which helps overcome the limitation of MFEM where artificial localised boundary conditions are employed. It has been demonstrated numerically that the proposed iterative algorithm converges to C^2-continuous solutions. This feature is very useful especially in subsurface flow simulations where the velocity field has to be continuous across the coarse cell interfaces to ensure a conservative flow field. The scalability and high efficiency of the proposed algorithm has been confirmed against the performance of the fine

32

scale solver.

References

Aarnes, J.; Kippe, V.; Lie, K.-A. (2005): Mixed multiscale finite elements and streamline methods for reservoir simulation of large geomodels. *Advances in Water Resources*, vol. 28, pp. 257–271.

Allaire, G.; Brizzi, R. (2005): A multiscale finite element method for numerical homogenization. *Multiscale Modeling & Simulation*, vol. 43, pp. 790–812.

An-Vo, D.-A.; Mai-Duy, N.; Tran, C.-D.; Tran-Cong, T. (2012): Modeling strain localisation in a segmented bar by a C^2-continuous two-node integrated-RBF element formulation. *Boundary Element and Other Mesh Reduction Method XXXIV*, vol. 53, pp. 3–13.

An-Vo, D.-A.; Mai-Duy, N.; Tran, C.-D.; Tran-Cong, T. (2013): ADI method based on C^2-continuous two-node integrated-RBF elements for viscous flows. *Applied Mathematical Modelling*, vol. 37, pp. 5184–5203.

An-Vo, D.-A.; Mai-Duy, N.; Tran-Cong, T. (2010): Simulation of Newtonian-fluid flows with C^2-continuous two-node integrated-RBF elements. *Structural Longevity*, vol. 4(1), pp. 39–45.

An-Vo, D.-A.; Mai-Duy, N.; Tran-Cong, T. (2011): A C^2-continuous control-volume technique based on Cartesian grids and two-node integrated-RBF elements for second-order elliptic problems. *CMES: Computer Modeling in Engineering and Sciences*, vol. 72 (4), pp. 299–334.

An-Vo, D.-A.; Mai-Duy, N.; Tran-Cong, T. (2011): High-order upwind methods based on C^2-continuous two-node integrated elements for viscous flows. *CMES: Computer Modeling in Engineering and Sciences*, vol. 80 (2), pp. 141–177.

Arbogast, T. (2002): Implementation of a locally conservative numerical subgrid upscaling scheme for two-phase Darcy flow. *Computational Geosciences*, vol. 6, pp. 453–481.

Babuška, I.; Caloz, G.; Osborn, J. (1994): Special finite element methods for a class of second order elliptic problems with rough coefficients. *SIAM J. on Numerical Analysis*, vol. 31, pp. 945–981.

Burnett, D. S. (1987): *Finite element analysis from concepts to applications*. Addison-Wesley Publishing company.

Chen, Z.; Hou, T. Y. (2002): A mixed multiscale finite element method for elliptic problems with oscillating coefficients. *Mathematics of Computation*, vol. 72 (242), pp. 541–576.

Chu, J.; Efendiev, Y.; Ginting, V.; Hou, T. (2008): Flow based oversampling technique for multiscale finite element methods. *Advances in Water Resources*, vol. 31, pp. 599–608.

Dykaar, B. B.; Kitanidis, P. K. (1992): Determination of the effective hydraulic conductivity for heterogeneous porous media using a numerical spectral approach 1. method. *Water Resources Research*, vol. 28, pp. 1155–1166.

Fasshauer, G. (2007): *Meshfree Approximation Methods With Matlab*. World Scientific Publishers: Singapore.

Hajibeygi, H.; Bonfigli, G.; Hesse, M. A.; Jenny, P. (2008): Iterative multiscale finite-volume method. *Journal of Computational Physics*, vol. 227, pp. 8604–8621.

Hajibeygi, H.; Jenny, P. (2009): Multiscale finite-volume method for parabolic problems arising from compressible multiphase flow in porous media. *Journal of Computational Physics*, vol. 228(14), pp. 5129–5147.

Hajibeygi, H.; Jenny, P. (2011): Adaptive iterative multiscale finite volume method. *Journal of Computational Physics*, vol. 230(3), pp. 628–643.

Hajibeygi, H.; Karvounis, D.; Jenny, P. (2011): A hierarchical fracture model for the iterative multiscale finite volume method. *Journal of Computaional Physics*, vol. 230(24), pp. 8729–8743.

Hou, T. Y. (2005): Multiscale modelling and computation of fluid flow. *Int. J. for Numerical Methods in Fluids*, vol. 47, pp. 707–719.

Hou, T. Y.; Wu, X.-H. (1997): A multiscale finite element method for elliptic problems in composite materials and porous media. *Journal of Computational Physics*, vol. 134, pp. 169–189.

Hou, T. Y.; Wu, X.-H.; Cai, Z. (1999): Convergence of a multiscale finite element method for elliptic problems with rapidly oscillating coefficients. *Mathematics of Computation*, vol. 68 (227), pp. 913–943.

34

Jenny, P.; Lee, S. H.; Tchelepi, H. A. (2003): Multi-scale finite-volume method for elliptic problems in subsurface flow simulation. *Journal of Computational Physics*, vol. 187, pp. 47–67.

Jenny, P.; Lee, S. H.; Tchelepi, H. A. (2004): Adaptive multiscale finite-volume method for multiphase flow and transport in porous media. *Multiscale Modelling and Simulation*, vol. 3 (1), pp. 50–64.

Jenny, P.; Lee, S. H.; Tchelepi, H. A. (2006): Adaptive fully implicit multi-scale finite-volume method for multi-phase flow and transport in heterogenous porous media. *Journal of Computational Physics*, vol. 217(2), pp. 627–641.

Kansa, E. (1990): Multiquadrics-a scattered data approximation scheme with applications to computational fluid-dynamics-II. *Computers & Mathematics with Applications*, vol. 19, pp. 147–161.

Lunati, I.; Jenny, P. (2006): Multiscale finite-volume method for compressible multiphase flow in porous media. *Journal of Computational Physics*, vol. 216, pp. 616–636.

Lunati, I.; Jenny, P. (2006): The multiscale finite-volume method - a flexible tool to model physically complex flow in porous media. *in: Proceeding of European Conference of Mathematics of Oil Recovery X*.

Lunati, I.; Jenny, P. (2008): Multiscale finite-volume method for density-driven flow in porous media. *Computational Geosciences*, vol. 12, pp. 337–350.

Mai-Duy, N.; Tanner, R. I. (2007): A collocation method based on one-dimensional RBF interpolation scheme for solving PDEs. *International Journal of Numerical Methods for Heat & Fluid Flow*, vol. 17(2), pp. 165–186.

Mai-Duy, N.; Tran-Cong, T. (2001): Numerical solution of differential euqations using multiquadric radial basis function networks. *Neural Networks*, vol. 14, pp. 185–199.

Mai-Duy, N.; Tran-Cong, T. (2003): Approximation of function and its derivatives using radial basis function network methods. *Applied Mathematical Modelling*, vol. 27, pp. 197–220.

Mai-Duy, N.; Tran-Cong, T. (2008): A multidomain integrated-radial-basis-function collocation method for elliptic problems. *Numerical Methods for Partial Differential Equations*, vol. 24, pp. 1301–1320.

Mai-Duy, N.; Tran-Cong, T. (2009): A Cartesian-grid discretisation scheme based on local integrated RBFNs for two-dimensional elliptic problems. *CMES: Computer Modeling in Engineering & Sciences*, vol. 51, pp. 213–238.

Mai-Duy, N.; Tran-Cong, T. (2010): A numerical study of 2D integrated RBFNs incorporating Cartesian grids for solving 2D elliptic differential problems. *Numerical Methods for Partial Differential Equations*, vol. 26 (6), pp. 1443–1462.

McCarthy, J. (1995): Comparison of fast algorithms for estimating large-scale permeabilities of heterogeneous media. *Transport in Porous Media*, vol. 19, pp. 123–137.

Wang, W.; Guzman, J.; Shu, C.-W. (2011): The multiscale discontinuous Galerkin method for solving a class of second order elliptic problems with rough coefficients. *International Journal of Numerical Analysis and Modeling*, vol. 8 (1), pp. 28–47.

Wang, W.; Shu, C.-W. (2009): The WKB local discontinuous Galerkin method for the simulation of Schrödinger equation in a resonant tunneling diode. *Journal of Scientific Computing*, vol. 40, pp. 360–374.

Table 1: One-dimensional example 1, $\varepsilon = 0.01$, Strategy 1: L_2 errors of the field variable, its first and second derivatives. It is noted that the set of test nodes contains $10,001$ uniformly distributed points. LCR stands for local convergence rate and [*] is Wang, Guzman, and Shu (2011).

| | MFEM | | | Present method | | | | | |
| | $\varepsilon = 0.01, N = 11$ | | | | | | | | |
Local fine grid (n)	$Ne(u)$	LCR		$Ne(u)$	LCR	$Ne(\mathrm{d}u/\mathrm{d}x)$	LCR	$Ne(\mathrm{d}^2u/\mathrm{d}x^2)$	LCR
21	1.30E-02	-		4.10E-03	-	1.16E-01	-	5.37E-01	-
41	1.22E-02	0.09		3.60E-04	3.51	2.44E-02	2.25	2.19E-01	1.29
61	1.21E-02	0.02		6.76E-05	4.12	5.80E-03	3.54	8.21E-02	2.42
81	1.21E-02	0.00		2.11E-05	4.05	2.13E-03	3.48	4.14E-02	2.38
101	1.21E-02	0.00		8.63E-06	4.01	9.90E-04	3.43	2.50E-02	2.26
121	1.21E-02	0.00		4.18E-06	3.98	5.34E-04	3.39	1.62E-02	2.38
141	1.21E-02	0.00		2.28E-06	3.93	3.18E-04	3.36	1.16E-02	2.17
161	1.21E-02	0.00		1.35E-06	3.92	2.04E-04	3.32	8.47E-03	2.36
181	1.21E-02	0.00		8.53E-07	3.90	1.39E-04	3.26	6.56E-03	2.17
	$O(h^{0.03})$			$O(h^{3.91})$		$O(h^{3.16})$		$O(h^{2.09})$	
Wang et al. (S^1) [*]				1.03E-03		4.73E-02			
Wang et al. (S^2) [*]				1.16E-05		1.01E-03			

Table 2: One-dimensional example 1, $\varepsilon = 0.01$, Strategy 2: L_2 errors of the field variable, its first and second derivatives. It is noted that the set of test nodes contains $10,001$ uniformly distributed points. LCR stands for local convergence rate

| | | | $\varepsilon = 0.01, n = 27$ | | | | | |
| | MFEM | | Present method | | | | | |
Coarse grid (N)	$Ne(u)$	LCR	$Ne(u)$	LCR	$Ne(\mathrm{d}u/\mathrm{d}x)$	LCR	$Ne(\mathrm{d}^2u/\mathrm{d}x^2)$	LCR
11	1.25E-2	-	2.06E-3	-	1.09E-1	-	5.90E-1	-
21	2.63E-3	2.25	8.91E-5	4.53	1.26E-2	3.11	1.49E-1	1.99
31	1.66E-3	1.14	3.52E-4	-3.39	5.97E-3	1.84	1.09E-1	0.77
41	9.63E-4	1.89	1.98E-4	2.00	1.65E-3	4.47	3.64E-2	3.80
51	7.36E-4	1.20	3.93E-6	17.57	7.79E-4	3.37	2.32E-2	2.02
61	3.71E-4	3.76	2.40E-5	-9.92	1.43E-3	-3.33	5.26E-2	-4.49
71	2.74E-4	1.98	1.43E-5	3.36	9.88E-4	2.40	4.38E-2	1.18
81	2.12E-4	1.93	8.44E-6	3.94	8.42E-4	1.20	3.96E-2	0.76
91	1.83E-4	1.22	6.86E-6	1.76	6.13E-4	2.70	3.44E-2	1.19
101	9.12E-4	-15.24	2.53E-7	31.31	1.01E-4	17.12	5.82E-3	16.86
	$O(H^{1.61})$		$O(H^{3.03})$		$O(H^{2.51})$		$O(H^{1.47})$	

Table 3: One-dimensional example 2, $\varepsilon = 0.01$, Strategy 1: L_2 errors of the field variable, its first and second derivatives by the present method. It is noted that the set of test nodes contains $100,001$ uniformly distributed points. LCR stands for local convergence rate.

Local fine grid (n)	$\varepsilon = 0.01, N = 51$					
	$Ne(u)$	LCR	$Ne(\mathrm{d}u/\mathrm{d}x)$	LCR	$Ne(\mathrm{d}^2u/\mathrm{d}x^2)$	LCR
21	2.59E-2	-	1.18E-1	-	5.33E-1	-
41	2.19E-3	3.56	2.45E-2	2.27	2.16E-1	1.30
61	4.02E-4	4.18	5.77E-3	3.57	8.07E-2	2.43
81	1.25E-4	4.06	2.10E-3	3.51	4.07E-2	2.38
101	5.11E-5	4.01	9.69E-4	3.47	2.42E-2	2.33
121	2.49E-5	3.94	5.19E-4	3.42	1.59E-2	2.30
141	1.36E-5	3.92	3.07E-4	3.41	1.12E-2	2.27
161	8.09E-6	3.89	1.96E-4	3.36	8.32E-3	2.23
181	5.14E-6	3.85	1.32E-4	3.36	6.44E-3	2.17
201	3.43E-6	3.84	9.30E-5	3.32	5.23E-3	1.98
241	1.72E-6	3.79	5.11E-5	3.28	3.46E-3	2.27
281	9.62E-7	3.77	3.11E-5	3.22	2.50E-3	2.11
	$O(h^{3.91})$		$O(h^{3.24})$		$O(h^{2.13})$	

Table 4: One-dimensional example 2, $\varepsilon = 0.01$, Strategy 2: L_2 errors of the field variable, its first and second derivatives by the present method. It is noted that the set of test nodes contains $100,001$ uniformly distributed points. LCR stands for local convergence rate.

Coarse grid (N)	$\varepsilon = 0.01$, $n = 101$					
	$Ne(u)$	LCR	$Ne(\mathrm{d}u/\mathrm{d}x)$	LCR	$Ne(\mathrm{d}^2u/\mathrm{d}x^2)$	LCR
11	3.66E-2	-	7.81E-2	-	3.53E-1	-
21	1.35E-3	4.76	1.83E-2	2.09	1.66E-1	1.09
31	5.86E-3	-3.62	6.85E-3	2.42	7.72E-2	1.89
41	1.18E-3	5.57	2.58E-3	3.39	3.82E-2	2.45
51	5.11E-5	14.07	9.69E-4	4.39	2.42E-2	2.05
61	1.72E-4	-6.66	1.29E-3	-1.57	3.60E-2	-2.18
71	1.13E-4	2.73	9.39E-4	2.06	3.06E-2	1.05
81	5.82E-5	4.97	7.20E-4	1.99	2.66E-2	1.05
91	2.71E-5	6.49	4.08E-4	4.82	1.74E-2	3.60
101	7.86E-7	33.60	1.20E-4	11.62	6.16E-3	9.86
	$O(H^{3.71})$		$O(H^{2.55})$		$O(H^{1.49})$	

Table 5: Two-dimensional example 1: L_2 errors of the field variable, its first and second derivatives. LCR stands for local convergence rate.

			Strategy 1, $N \times N = 5 \times 5$					
	MFEM		Present method					
Fine scale grid ($n \times n$)	$Ne(u)$	LCR	$Ne(u)$	LCR	$Ne(\partial u/\partial x)$	LCR	$Ne(\partial u/\partial y)$	LCR
11×11	5.54E-2	-	1.73E-5	-	5.48E-5	-	5.49E-5	-
21×21	5.54E-2	0.00	4.76E-6	1.86	1.47E-5	1.90	1.46E-5	1.91
31×31	5.54E-2	0.00	2.21E-6	1.89	6.68E-6	1.94	6.68E-6	1.94
41×41	5.54E-2	0.00	1.28E-6	1.91	3.81E-6	1.95	3.81E-6	1.95
51×51	5.54E-2	0.00	8.30E-7	1.93	2.46E-6	1.96	2.46E-6	1.96
61×61	5.54E-2	0.00	5.83E-7	1.94	1.72E-6	1.97	1.72E-6	1.97
71×71	5.54E-2	0.00	4.32E-7	1.94	1.27E-6	1.97	1.27E-6	1.97
81×81	5.54E-2	0.00	3.33E-7	1.95	9.75E-7	1.97	9.75E-7	1.97
91×91	5.54E-2	0.00	2.65E-7	1.94	7.75E-7	1.96	7.75E-7	1.96
	$O(h^{0.00})$		$O(h^{1.90})$		$O(h^{1.94})$		$O(h^{1.94})$	
Coarse grid ($N \times N$)			Strategy 2, $n \times n = 11 \times 11$					
5×5	5.54E-2	-	1.73E-5	-	5.48E-5	-	5.49E-5	-
9×9	1.40E-2	1.99	1.09E-6	3.99	6.99E-6	2.97	6.99E-6	2.97
13×13	6.23E-3	2.00	2.09E-7	4.07	2.31E-6	2.73	2.31E-6	2.73
17×17	3.51E-3	2.00	6.54E-8	4.04	1.33E-6	1.92	1.33E-6	1.92
21×21	2.25E-3	2.00	2.67E-8	4.01	1.03E-6	1.15	1.03E-6	1.15
25×25	1.56E-3	2.00	1.29E-8	3.99	8.85E-7	0.83	8.85E-7	0.83
29×29	1.15E-3	2.00	7.04E-9	3.93	7.86E-7	0.77	7.86E-7	0.77
33×33	8.78E-4	2.00	4.17E-9	3.92	7.04E-7	0.83	7.04E-7	0.83
37×37	6.94E-4	2.00	2.63E-9	3.91	6.33E-7	0.90	6.33E-7	0.90
	$O(H^{2.00})$		$O(H^{4.01})$		$O(H^{1.97})$		$O(H^{1.97})$	

Table 6: Two-dimensional example 2, $\varepsilon = 0.1$: L_2 errors of the field variable, its first and second derivatives. LCR stands for local convergence rate.

| Local fine grid ($n \times n$) | MFEM | | Present method | | | | | |
	$Ne(u)$	LCR	$Ne(u)$	LCR	$Ne(\partial u/\partial x)$	LCR	$Ne(\partial u/\partial y)$	LCR
			Strategy 1, $N \times N = 5 \times 5$					
11×11	4.13E-1	-	5.01E-5	-	1.49E-4	-	1.49E-4	-
21×21	4.14E-1	0.00	3.55E-6	3.82	1.14E-5	3.71	1.13E-5	3.72
31×31	4.15E-1	0.00	8.51E-7	3.52	2.95E-6	3.33	2.95E-6	3.31
41×41	4.15E-1	0.00	3.37E-7	3.22	1.26E-6	2.96	1.26E-6	2.96
51×51	4.15E-1	0.00	1.75E-7	2.94	6.86E-7	2.72	6.86E-7	2.72
61×61	4.15E-1	0.00	1.07E-7	2.70	4.33E-7	2.52	4.33E-7	2.52
71×71	4.15E-1	0.00	7.15E-8	2.62	2.99E-7	2.40	2.99E-7	2.40
81×81	4.15E-1	0.00	5.15E-8	2.46	2.19E-7	2.33	2.19E-7	2.33
91×91	4.15E-1	0.00	3.90E-8	2.36	1.68E-7	2.25	1.68E-7	2.25
	$O(h^{0.00})$		$O(h^{3.24})$		$O(h^{3.05})$		$O(h^{3.05})$	
Coarse grid ($N \times N$)			Strategy 2, $n \times n = 11 \times 11$					
5×5	4.13E-1	-	5.01E-5	-	1.49E-4	-	1.49E-4	-
9×9	1.15E-1	1.84	3.99E-6	3.65	1.06E-5	3.81	1.06E-5	3.81
13×13	5.19E-2	1.96	7.26E-7	4.20	7.30E-6	0.92	7.29E-6	0.92
17×17	2.94E-2	1.98	2.52E-7	3.68	6.38E-6	0.47	6.38E-6	0.46
21×21	1.89E-2	1.98	1.21E-7	3.29	5.76E-6	0.46	5.76E-6	0.46
25×25	1.31E-2	2.01	7.03E-8	2.98	5.22E-6	0.54	5.22E-6	0.54
29×29	9.64E-3	1.99	6.49E-8	0.52	4.72E-6	0.65	4.71E-6	0.67
33×33	7.39E-3	1.99	5.00E-8	1.95	4.26E-6	0.77	4.25E-6	0.77
37×37	5.84E-3	2.00	2.66E-8	5.36	3.84E-6	0.88	3.84E-6	0.86
	$O(H^{1.95})$		$O(H^{3.38})$		$O(H^{1.40})$		$O(H^{1.40})$	

Table 7: Two-dimensional example 2, $\varepsilon = 0.01$: L_2 errors of the field variable, its first and second derivatives. LCR stands for local convergence rate.

| | Strategy 1, $N \times N = 11 \times 11$ | | | | | | | |
| | MFEM | | Present method | | | | | |
Local fine grid ($n \times n$)	$Ne(u)$	LCR	$Ne(u)$	LCR	$Ne(\partial u/\partial x)$	LCR	$Ne(\partial u/\partial y)$	LCR
11×11	1.03E-1	-	1.93E-2	-	2.44E-2	-	2.44E-2	-
21×21	8.36E-2	0.30	9.83E-4	4.30	1.29E-3	4.24	1.29E-3	4.24
31×31	8.02E-2	0.10	1.80E-4	4.19	2.46E-4	4.09	2.45E-4	4.10
41×41	7.91E-2	0.05	5.49E-5	4.13	8.05E-5	3.88	7.80E-5	3.98
51×51	7.87E-2	0.02	2.20E-5	4.10	3.56E-5	3.66	3.54E-5	3.54
61×61	7.84E-2	0.02	1.06E-5	4.00	1.91E-5	3.42	1.90E-5	3.41
71×71	7.83E-2	0.01	5.73E-6	3.99	1.17E-5	3.18	1.17E-5	3.15
	$O(h^{0.13})$		$O(h^{4.17})$		$O(h^{3.94})$		$O(h^{3.95})$	
Coarse grid ($N \times N$)	Strategy 2, $n \times n = 11 \times 11$							
11×11	1.03E-1	-	1.93E-2	-	2.44E-2	-	2.44E-2	-
21×21	2.38E-2	2.11	3.91E-4	5.63	1.24E-3	4.30	1.25E-3	4.29
31×31	1.39E-2	1.33	1.82E-4	1.89	2.93E-4	3.56	2.92E-4	3.59
41×41	5.98E-3	2.93	2.08E-5	7.54	1.05E-4	3.57	1.05E-4	3.56
51×51	3.59E-3	2.29	5.09E-6	6.31	5.19E-5	3.16	5.22E-5	3.13
61×61	2.39E-3	2.23	1.63E-6	6.25	3.17E-5	2.70	3.19E-5	2.70
71×71	1.78E-3	1.91	9.05E-7	3.82	2.31E-5	2.05	2.32E-5	2.07
	$O(H^{2.10})$		$O(H^{5.12})$		$O(H^{3.60})$		$O(H^{3.59})$	
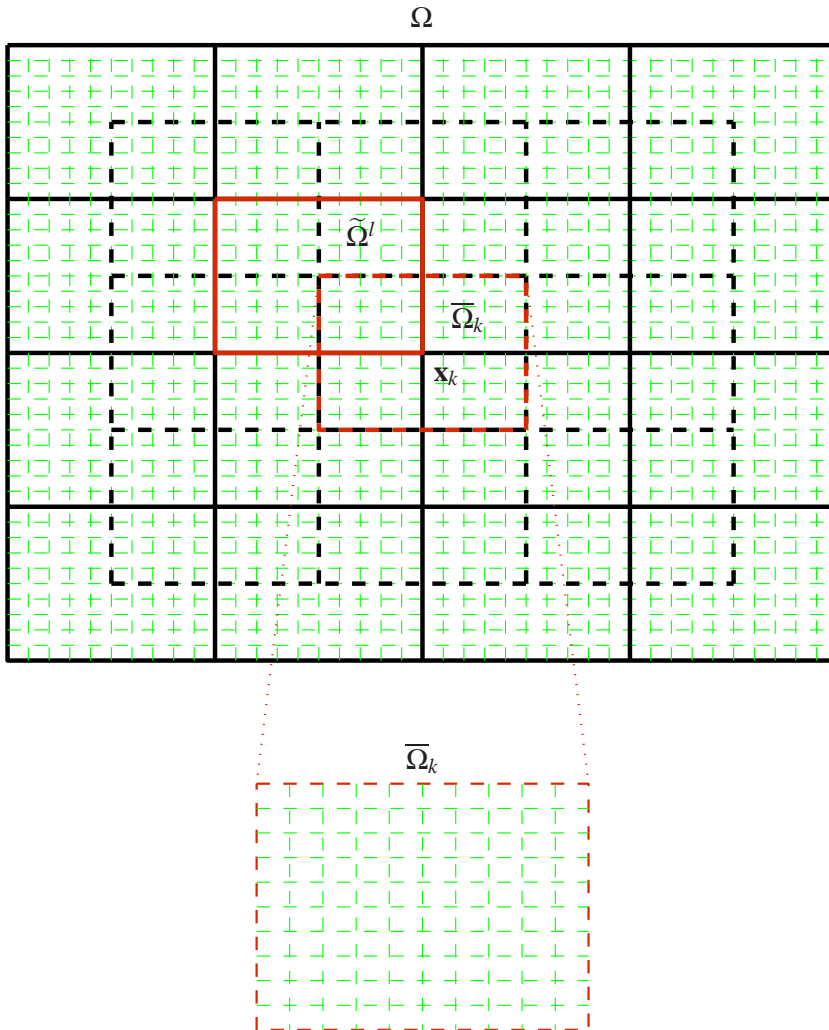
Figure 1: A computational domain Ω with the coarse grid (black dashed lines) and dual coarse grid (black solid lines); dashed and solid red lines indicate a selected control volume $\overline{\Omega}_k$ and a selected dual coarse cell $\widetilde{\Omega}^l$, respectively. Shown underneath is an enlarged control volume, on which is imposed a $n \times n = 11 \times 11$ local fine grid. It can be seen that the size of global fine grid (dashed green lines) is 41×41.
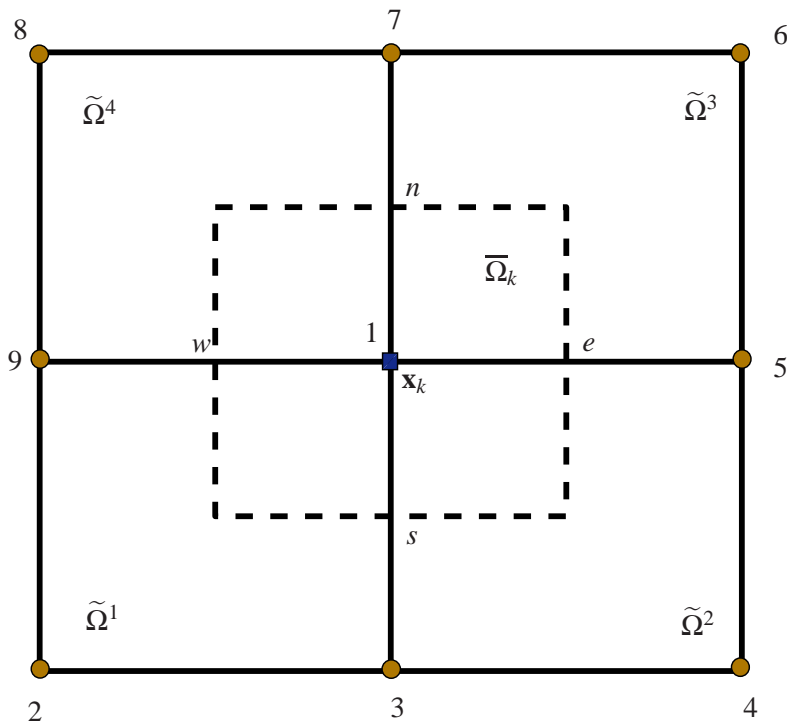
Figure 2: Local indices of dual cells and nodal points associated with a coarse grid node $\mathbf{x}_k$ and $\mathbf{x}_k \equiv \mathbf{x}_1$.

Interior grid node

Interior element

Ω

Semi-interior element

Boundary node
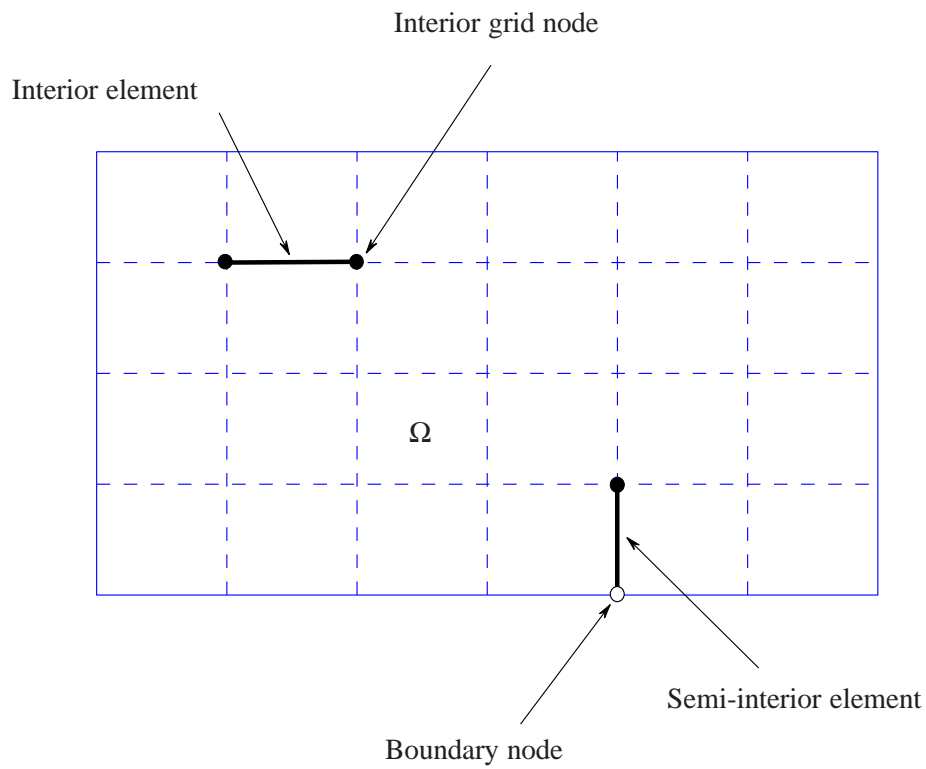
Figure 3: A domain is discretised by a Cartesian grid with interior and semi-interior elements.

(a) Interior element

(b) Semi-interior element

ϕ_1

ϕ_2

ϕ_b

ϕ_g

$\frac{\partial \phi_1}{\partial \eta}$

$\frac{\partial \phi_2}{\partial \eta}$

$\frac{\partial \phi_g}{\partial \eta}$

η

η
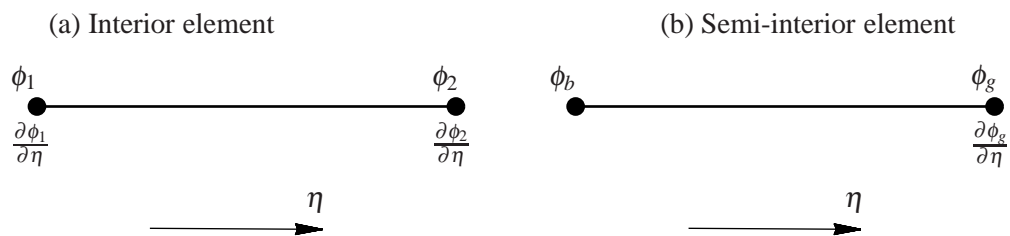
Figure 4: Schematic outline for 2-node IRBFEs.

46
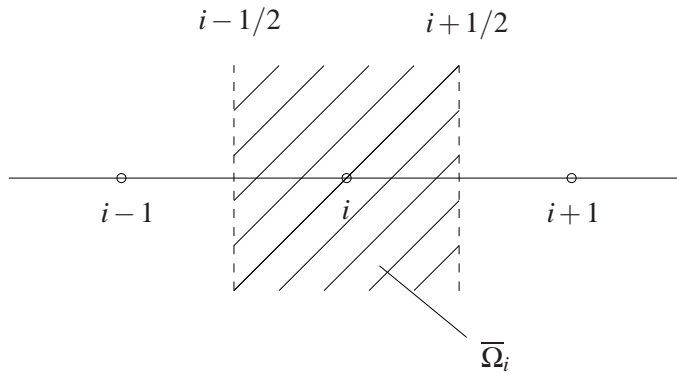
Figure 5: A CV discretisation scheme in 1D: node i and its associated control volume. The circles represent the nodes, and the vertical dash lines represent the faces of the control volume.
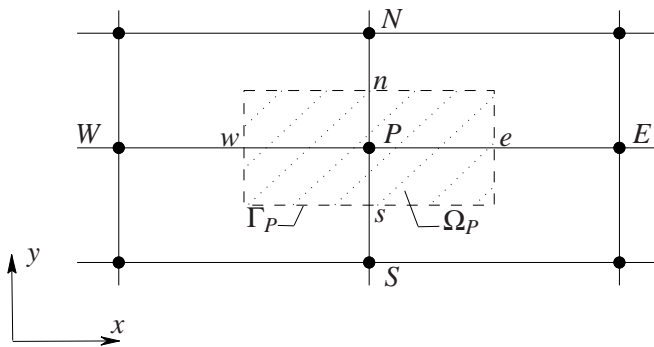
Figure 6: Schematic outline for a 2D control volume on the fine scale grid.
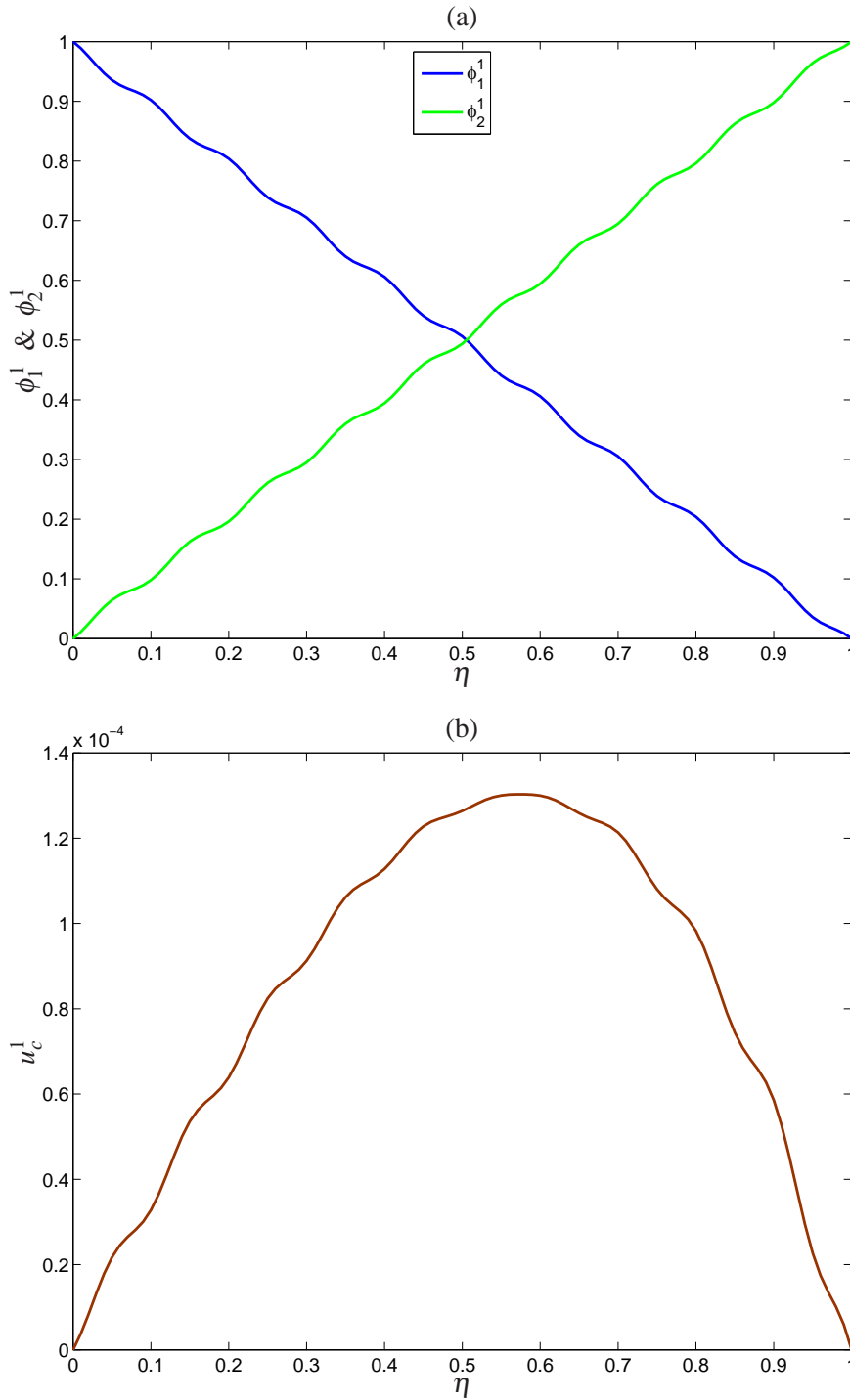
Figure 7: One-dimensional example 1, $\varepsilon = 0.01$, $N = 11$, $n = 101$: basis functions (a) and correction function (b) associated with the first coarse cell ($l = 1$). It is noted that the coarse cell is mapped to a unit length.

48
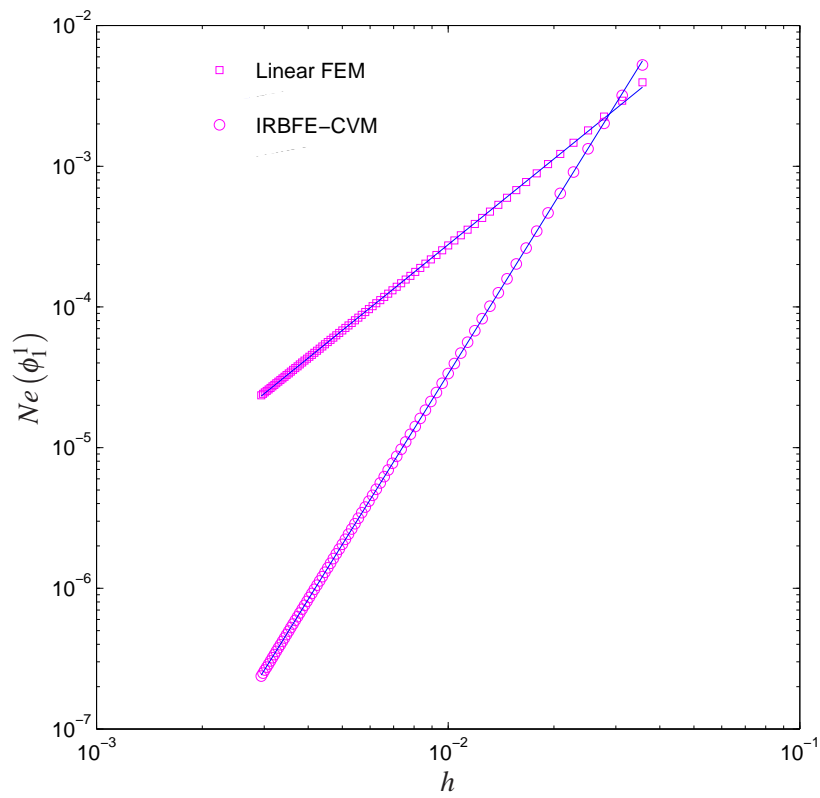
Figure 8: One-dimensional example 1: mesh convergence of a basis function.
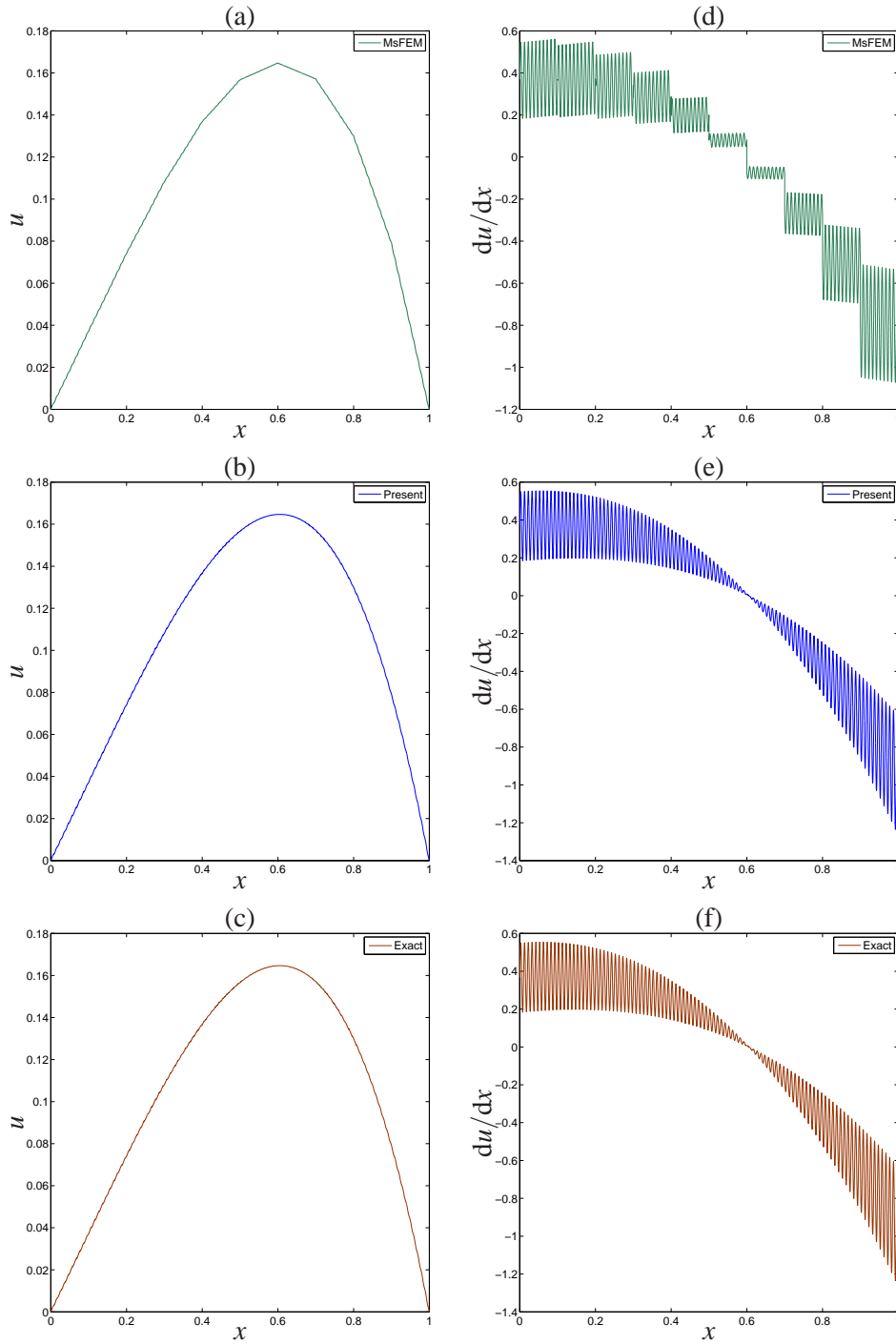
Figure 9: One-dimensional example 1, $\varepsilon = 0.01$, $N = 11$, $n = 101$: field variable and its first derivatives obtained by the present method in comparison with those obtained by MFEM and the exact solution.

50
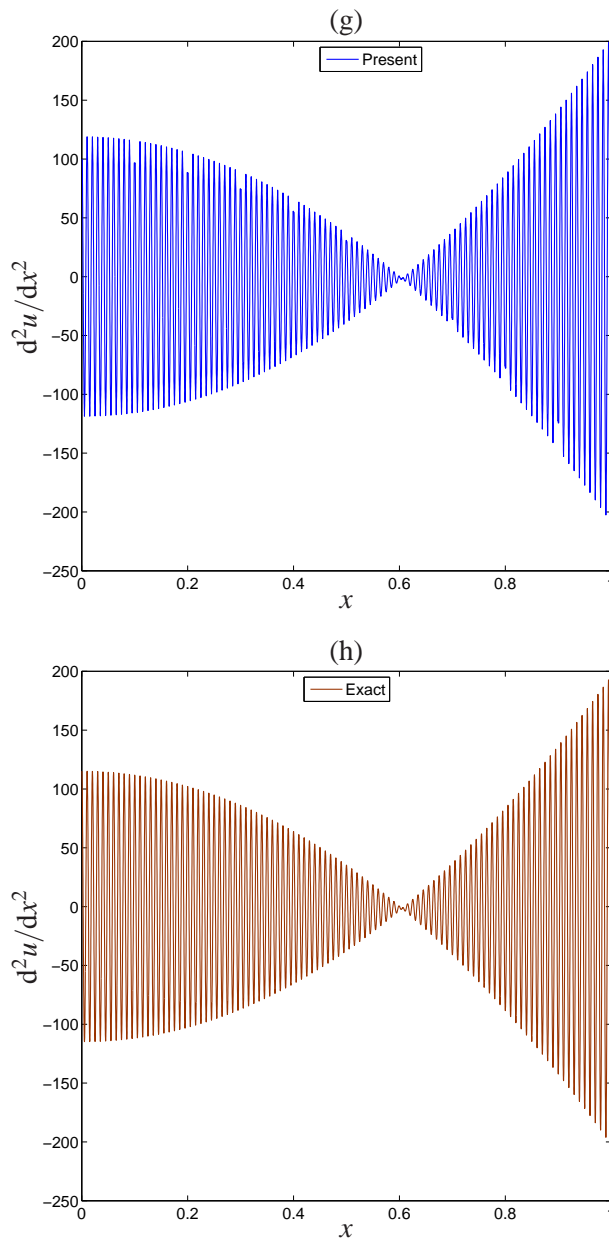
Figure 10: One-dimensional example 1, $\varepsilon = 0.01$, $N = 11$, $n = 101$: second derivatives obtained by the present method in comparison with that obtained by the exact solution.
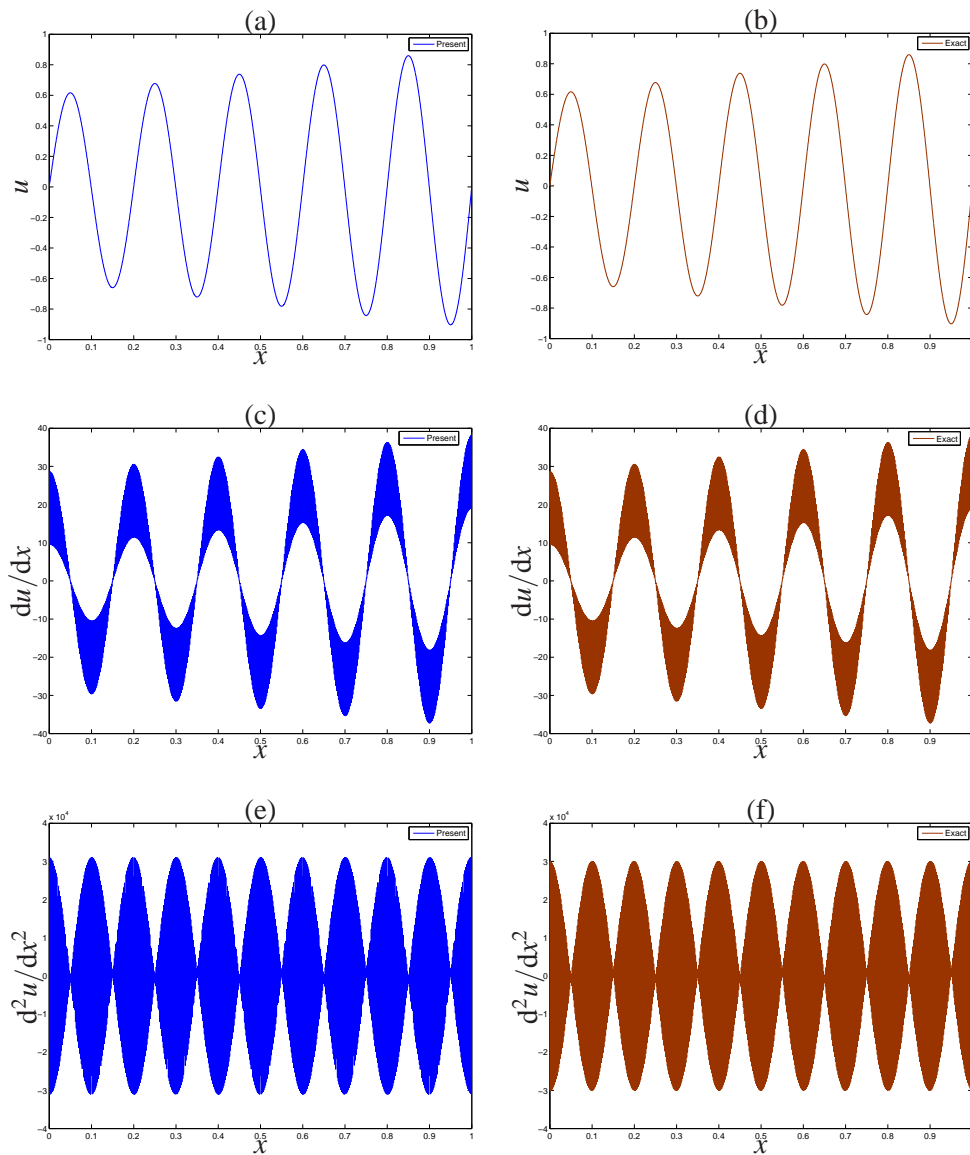
Figure 11: One-dimensional example 2, $\varepsilon = 0.01$, $N = 51$, $n = 101$: field variable, its first and second derivatives obtained by the present method in comparison with the exact solution.

52
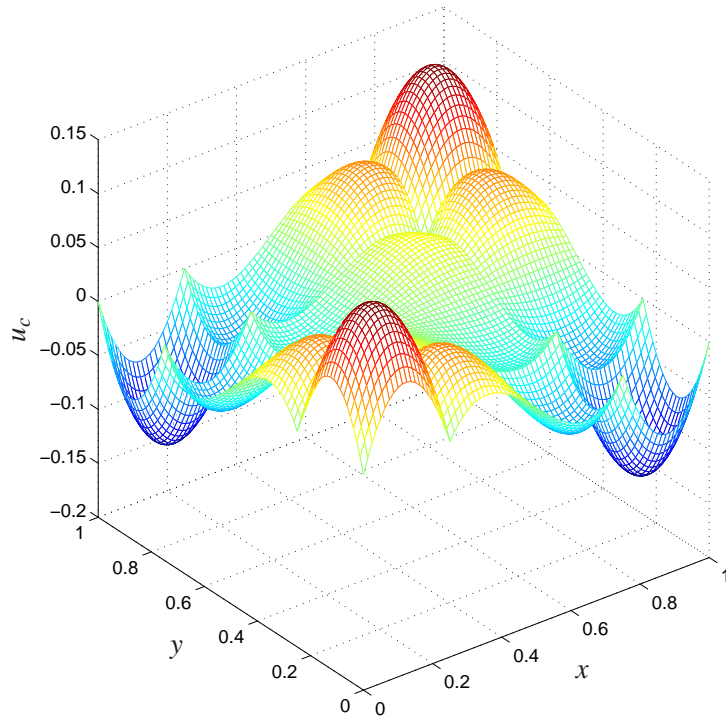
Figure 12: Two-dimensional example 1: collection of all correction functions on the problem domain obtained with a grid system of $N \times N = 5 \times 5$, $n \times n = 21 \times 21$.
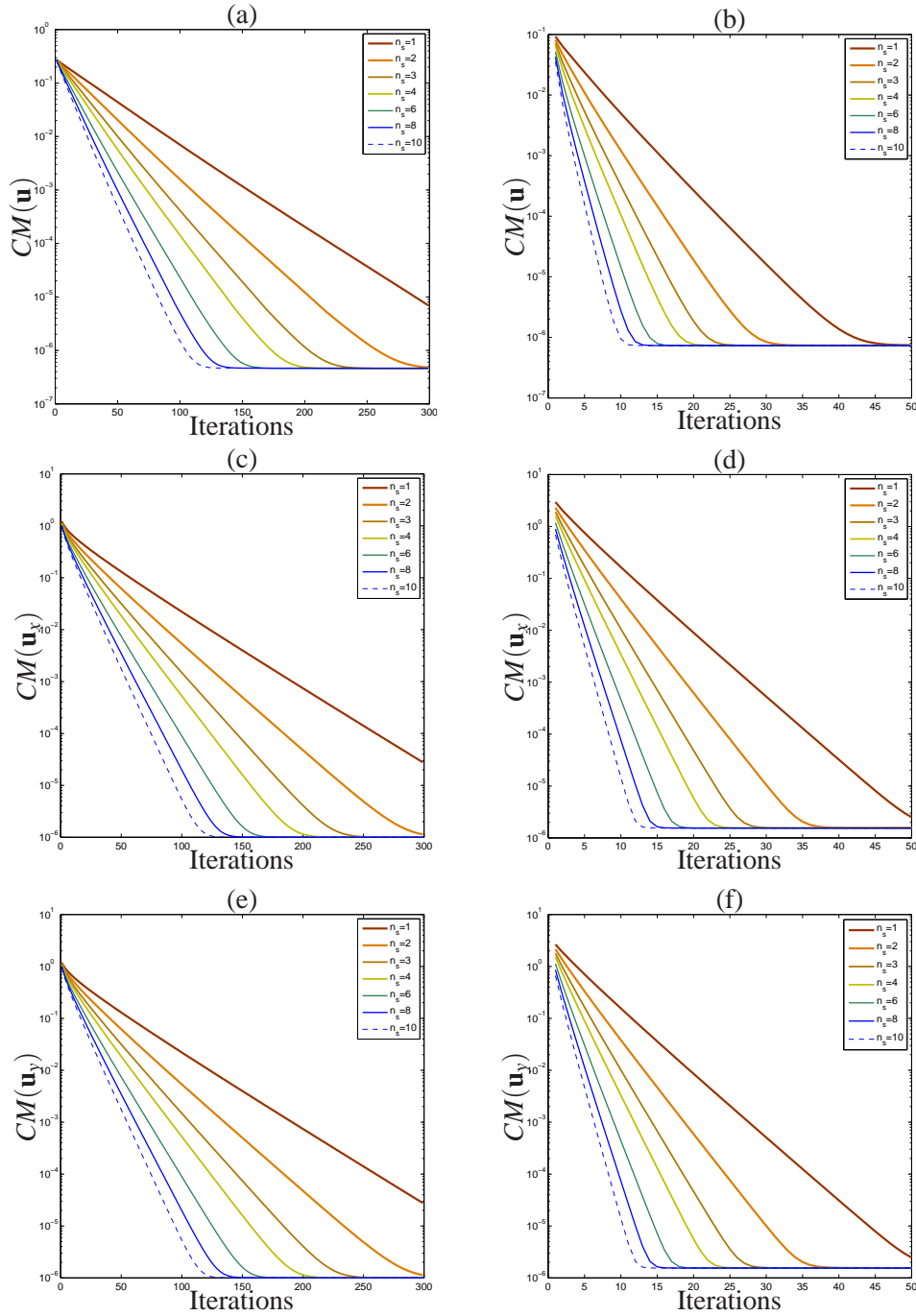
Figure 13: Two-dimensional example 1, $N \times N = 5 \times 5, n \times n = 81 \times 81$ (left) and $N \times N = 33 \times 33, n \times n = 11 \times 11$ (right): effect of the number of smoothing steps n_s on the convergence behaviour.

54

(a) $\varepsilon = 0.1$
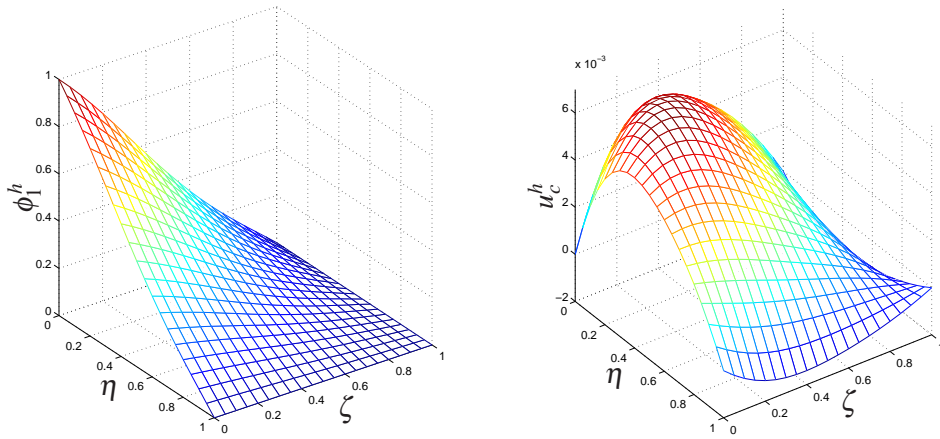
(b) $\varepsilon = 0.01$
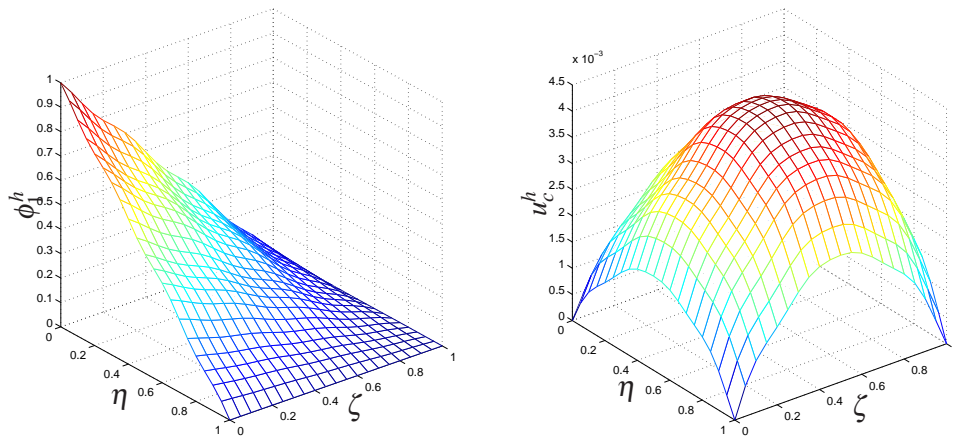
Figure 14: Two-dimensional example 2: typical basis and correction functions for the cases of $\varepsilon = 0.1$ using a grid system of $N \times N = 5 \times 5, n \times n = 21 \times 21$ and $\varepsilon = 0.01$ using a grid system of $N \times N = 11 \times 11, n \times n = 21 \times 21$.
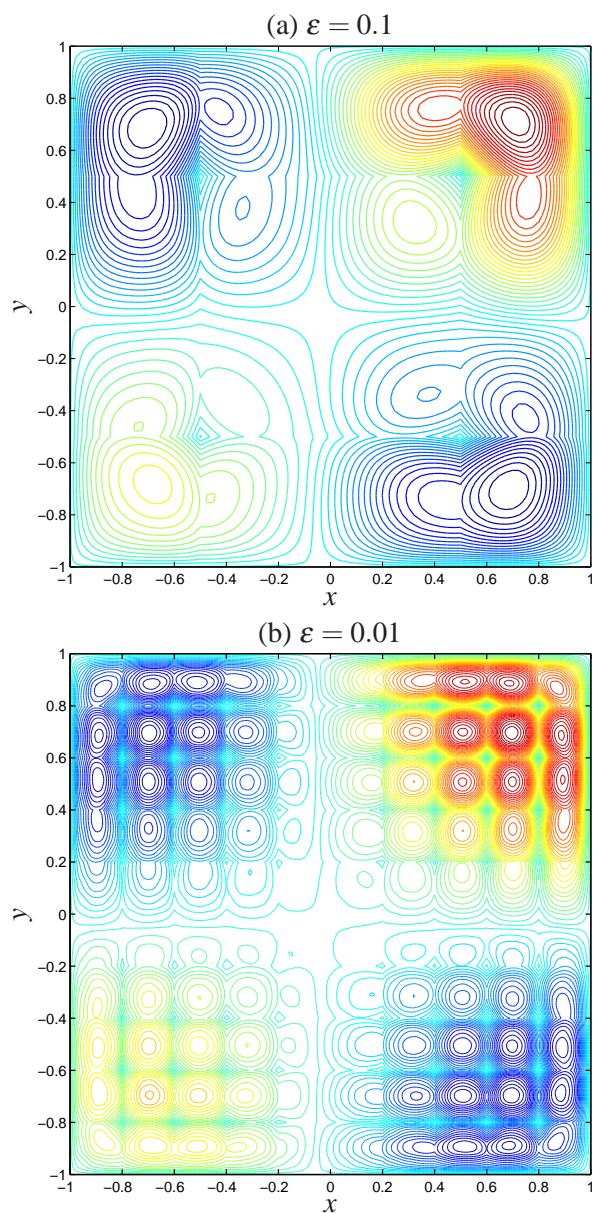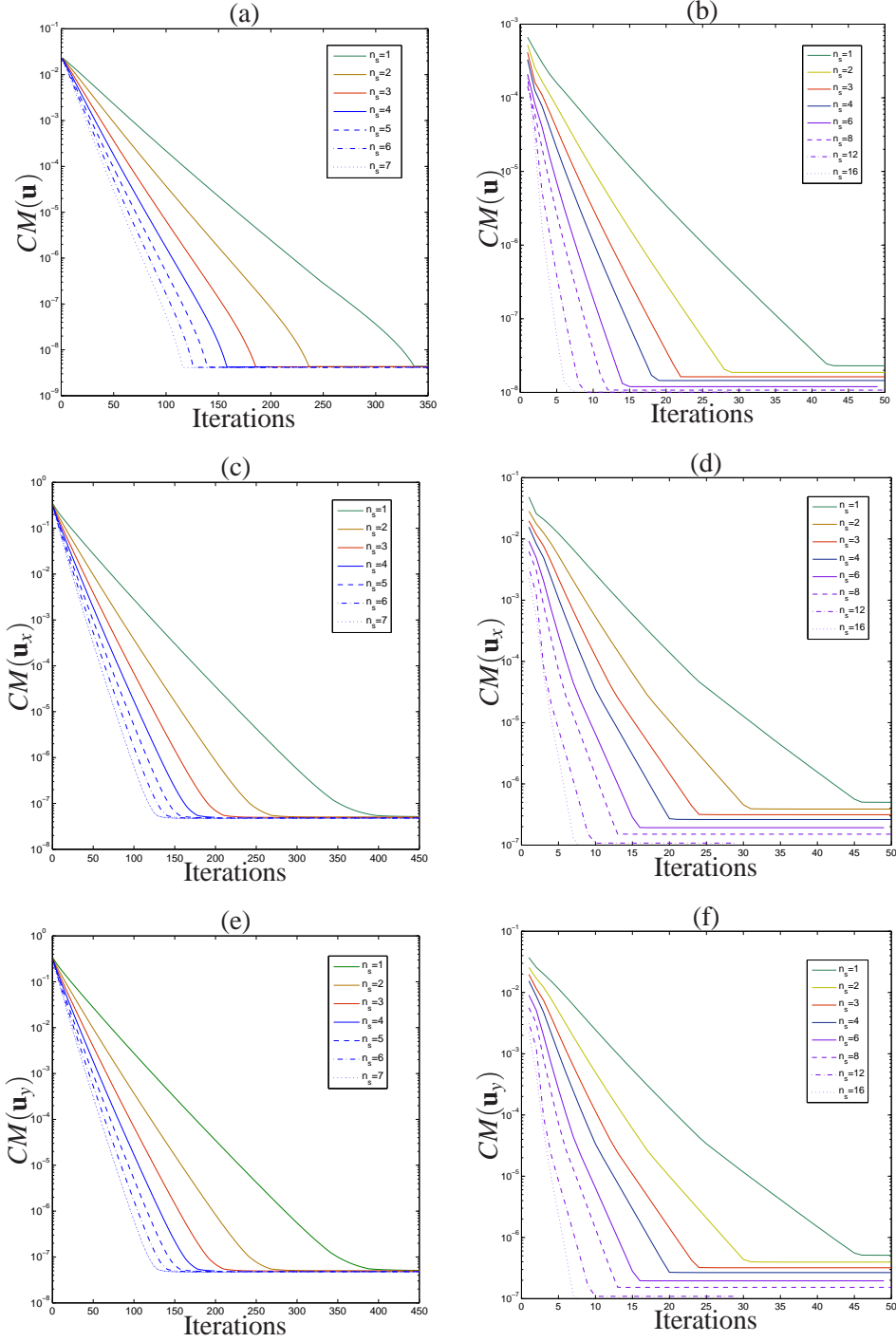
Figure 15: Two-dimensional example 2: contour plots of correction functions on the problem domain for the cases of $\varepsilon = 0.1$ using a grid system of $N \times N = 5 \times 5, n \times n = 21 \times 21$ and $\varepsilon = 0.01$ using a grid system of $N \times N = 11 \times 11, n \times n = 21 \times 21$.

56

Figure 16: Two-dimensional example 2, $\varepsilon = 0.1$, $N \times N = 5 \times 5, n \times n = 61 \times 61$ (left) and $N \times N = 25 \times 25, n \times n = 11 \times 11$ (right): effect of the number of smoothing steps n_s on the convergence behaviour.
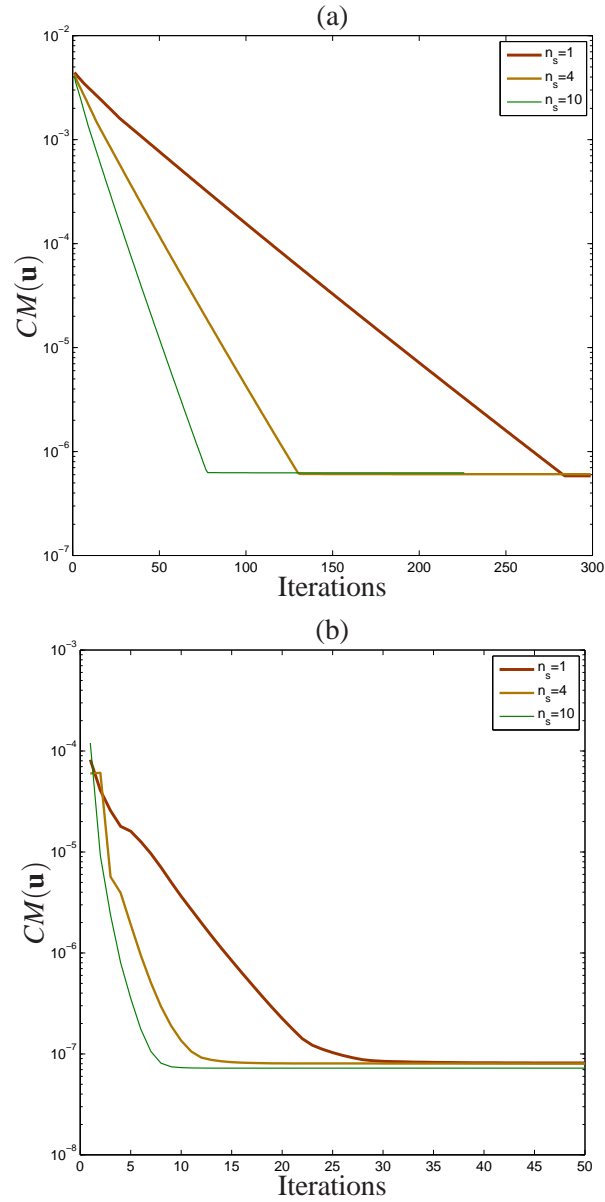
Figure 17: Two-dimensional example 2, $\varepsilon = 0.01$, $N \times N = 11 \times 11$, $n \times n = 71 \times 71$ (a) and $N \times N = 71 \times 71$, $n \times n = 11 \times 11$ (b): effect of the number of smoothing steps n_s on the convergence behaviour.
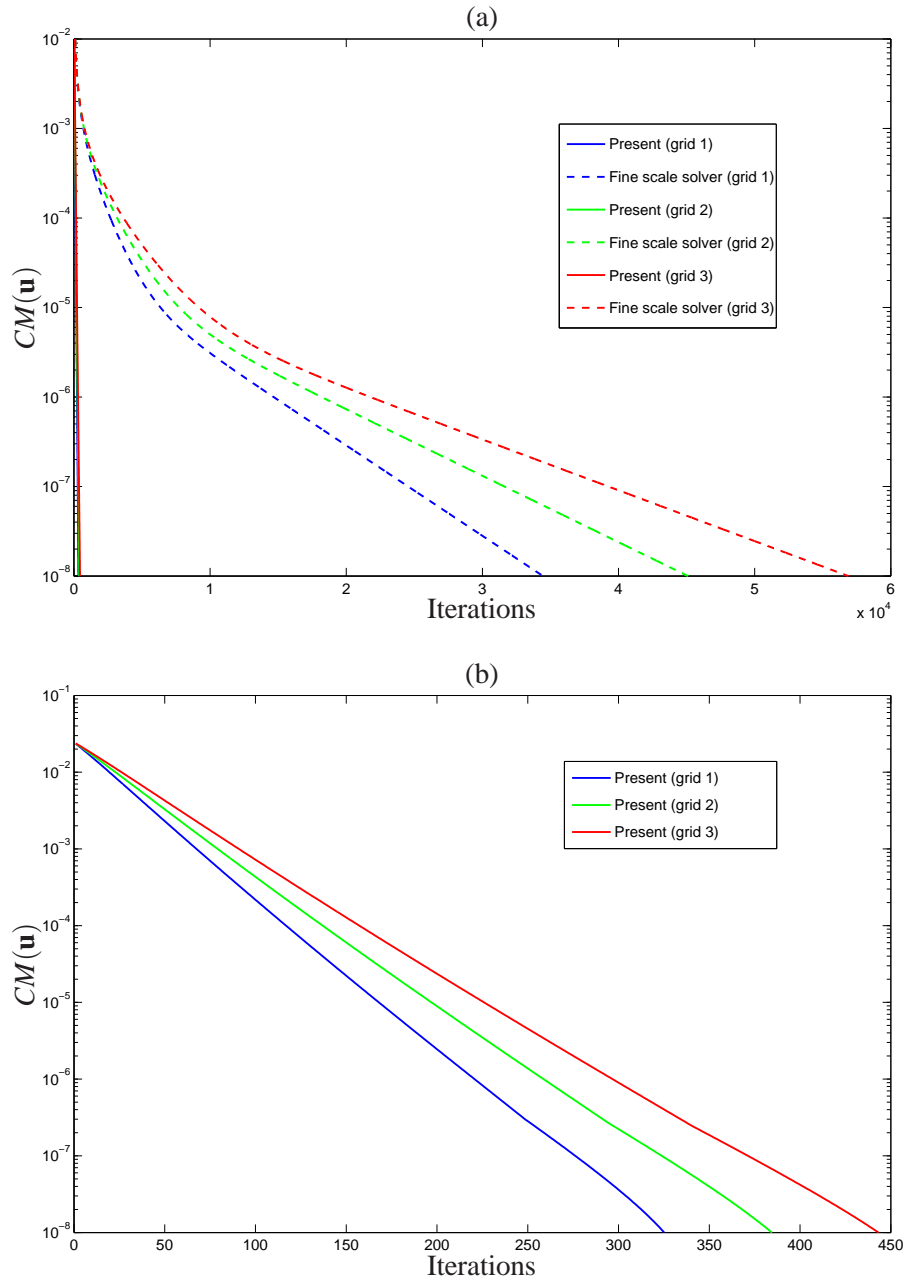
58

Figure 18: Two-dimensional example 2, $\varepsilon = 0.1$, $n_s = 1$: convergence of the present method and the fine scale solver with increasing sizes of the global fine grid; grid $1 = 241 \times 241$ ($N \times N = 5 \times 5, n \times n = 61 \times 61$), grid $2 = 281 \times 281$ ($N \times N = 5 \times 5, n \times n = 71 \times 71$), grid $3 = 321 \times 321$ ($N \times N = 5 \times 5, n \times n = 81 \times 81$).
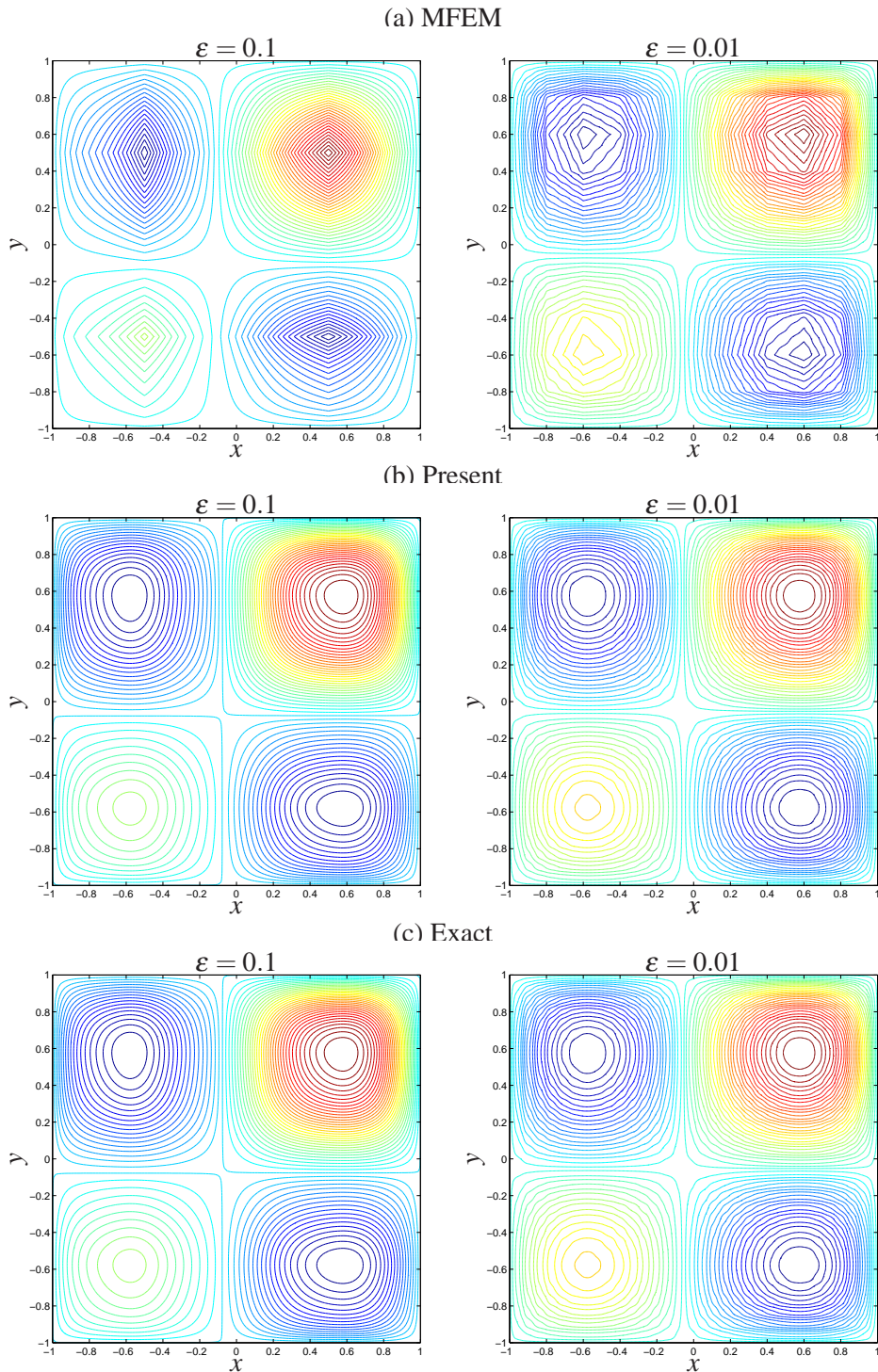
Figure 19: Two-dimensional example 2: contour plots of solutions for the cases of $\varepsilon = 0.1$ and $\varepsilon = 0.01$, the former is obtained with $N \times N = 5 \times 5, n \times n = 31 \times 31$ while the latter is obtained with $N \times N = 11 \times 11, n \times n = 31 \times 31$.